Optimising design parameters for offshore wind MP-TP wedge connection technology using analytical techniques

Helen Ryan [a], Alessandro Annoni [b], Jasper Winkes [c], Ali Mehmanparast [b,*]

[a] *Offshore Renewable Energy Engineering Centre, Cranfield University, Cranfield, MK43 0AL, UK*
[b] *Department of Naval Architecture, Ocean and Marine Engineering, University of Strathclyde, Glasgow, G1 1XQ, United Kingdom*
[c] *C1 Connections, Zuid Hollandlaan 7, The Hague, The Netherlands*

ARTICLE INFO

ABSTRACT

The offshore wind industry is a rapidly growing sector and will likely play a significant role in the future of green energy. Monopile support structures are the dominant foundation type in offshore wind turbines. Existing monopile to transition piece technologies have a number of challenges, and a new design, called wedge connection, presents a promising solution. In the present study analytical techniques, supported with finite element modelling, have been used to optimise the wedge connection design. A spring model was created and solved for both the application of the preload and the combination of the preload and the external force. A lower bound on the preload that would ensure the connection does not become loose was found. The self-locking mechanism was shown to be not a required design feature. The optimum number of wedge connections in one offshore wind turbine has been found as a function of the width of the connection and the monopile diameter. It has been shown that laboratory experiments on a single segment of wedge connection are likely to be conservative due to a higher stress concentration factor than in the full structure.

1. Introduction

1.1. An overview of offshore wind industry

Offshore wind has grown dramatically over the past two decades, increasing from less than 100 offshore wind turbines installed in fully commissioned wind farms in the year 2000 to over 7000 in 2020. The Levelised Cost of Energy (LCOE) for offshore wind has also fallen significantly, from 190 $/MWh in 2009 to 78 $/MWh in 2019 (Ryan and Mehmanparast, 2023). The UK is a world leader in offshore wind with the greatest number of installed offshore wind turbines globally, at 32% of installed turbines (Soares-Ramos et al., 2020). In early 2022, the UK raised its target for the amount of energy that will be produced from offshore wind by 2030 to 50 GW; enough energy to power every home in the country (UK, 2022). Other countries are becoming increasingly competitive in the offshore wind market with China top of the leader board for the new annual installed capacity in every year since 2017 (GWEC, 2021), and a current share of 26% of installed turbines. Other countries with a significant industry include Germany (20%), Denmark (8%), Belgium (6%) and the Netherlands (5%) (Soares-Ramos et al., 2020).

Although the capacity of offshore wind is still dwarfed by that of onshore, with 29 GW and 621 GW of installed capacity at the start of 2020 in each industry, respectively (Sati and Verma, 2021), offshore wind has a number of advantages over its onshore counterpart. These include that the wind resource in the sea is higher than at coasts, the lower visual and acoustic impact which allows designs to focus on maximising the power extracted, more consistent and reliable energy, and the spaciousness of the environment, amongst others (Sánchez et al., 2019).

A critical part of offshore wind turbine design is the foundations, which can account for around 30% of total costs (Díaz and Soares, 2020). The foundations must be able to withstand the load of the turbines and the stresses induced by the harsh environment, providing a safe and reliable base. A number of different designs for offshore wind foundations have been implemented in the industry, influenced by factors such as the water depth and the local climate (Sánchez et al., 2019). Some of the main foundation designs are the following.

1. Monopile: A long steel cylinder, with typically 22–40m of embedment depth and 6–10m of diameter, that sits in the seabed. The tower can either be supported directly by the monopile, or by a transition piece which sits between the two. The monopile is a simple design

Nomenclature		LCOE	Levelised cost of energy
		MP	Monopile
α	The angle of the wedge in the wedge connection	MP-TP	Monopile to transition piece connection
B1	The upper block in a single wedge connection, treated as a spring	MP1	The portion of the monopile in a single wedge connection above the hole, treated as a spring
B2	The lower block in a single wedge connection, treated as a spring	MP2	The portion of the monopile in a single wedge connection below the hole and down to the ground, treated as a spring
d	Width of the hole in the wedge connection	m	Mass
D	Monopile diameter	n	Number of wedge connections in one structure
δ_i	The compression (or expansion) of spring i after application of preload	PL	The force induced in the spring system through preloading
$\widetilde{\delta}_i$	The compression (or expansion) of spring i after application of preload and external axial force	R_1	Inner radius of the monopile
		R_2	Outer radius of the monopile
FEM	Finite element modelling	SCF	Stress concentration factor
F_A	An external axial force applied to a single wedge connection	S11	Principle stress along x direction
		S22	Principle stress along y direction
F_U	Force exerted on a wedge by the upper block	S33	Principle stress along z direction
F_L	Force exerted on a wedge by the lower block	S_{max_33}	Maximal stress along z direction
F_P	Force exerted on a wedge by the bolt	S_{N_33}	Nominal stress along z direction
f_U	Frictional force on upper face of the wedge	σ	Stress
f_L	Frictional force on lower face of the wedge	TP	The portion of the transition piece in a single wedge connection, treated as a spring
g	Acceleration due to gravity	μ	Friction coefficient
K_i	The spring constant associated with spring i	W	Wedges in a single wedge connection, treated as a spring

that is relatively straightforward to install and is economical (Sánchez et al., 2019), (Wang et al., 2018), (Mehmanparast et al., 2017), (Anandavijayan et al., 2021), (Hu et al., 2020). Monopiles are typically used in water depths of up to 50m in recent years.

2. Jacket: Typically a lattice structure with three or four legs and a large base. Jacket is suitable for water depths of 30–80m. It is stiffer than the monopile foundation and hence has more resistance to environmental loading; however, its fabrication and installation are costly and it has high maintenance work (Hao and Liu, 2017).

3. Tripod: A foundation with an anchor pile that is driven into the seabed with an additional three legs. It is resistant to wave and current loading and is suitable for water depths of between 25 and 50m. On the other hand, it is time consuming to construct tripods and they are difficult to transport (Hao and Liu, 2017), which is why this concept is not used any longer in Europe.

4. Gravity-based structure: Heavily reinforced concrete foundations that rely on gravity to remain in place. These structures are very difficult to transport due to their size and weight, typically limiting their application to water depths less than 25m (Yu et al., 2015).

5. Floating: Consists of an anchoring system, a floating platform, and a transition piece upon which the tower is installed (Sánchez et al., 2019). A range of designs exist for floating foundations. They are still relatively new technologies but offer the potential for use in very deep waters (Díaz et al., 2022) (Arredondo-Galeana and Brennan, 2021) (Esteban et al., 2019).

Data on the foundation type in fully commissioned or decommissioned offshore wind farms can be found in the literature where the proportion of offshore wind turbines with monopile foundations is found to be between 71% and 86% of all global offshore wind turbines in fully commissioned or decommissioned wind farms. This aligns with the findings of the EWEA in 2015 who found the proportion in Europe to be 80% (EWEA, 2016). The existing data show that among all varieties of foundation types listed above, monopile is by far the dominant majority which has been used in current offshore wind farms around the world.

1.2. Monopile to transition piece connection technologies

In an offshore wind turbine with monopile foundation, there are

typically three main parts to the structure; the monopile, the tower and the transition piece which is the connection between the monopile and the tower. As well as simplifying the attachment of the monopile to the wind turbine, the transition piece absorbs tolerances of possible inclinations - in the presence of grouted connection - and typically includes a platform that can be linked to incoming vessels and allow inspection or maintenance crew to gain access (Mehmanparast et al., 2020). Traditionally, the connection technology used to join the monopile and the transition piece together was the grouted connection, and later the flanged bolted connection was introduced since installations could be faster and more cost-efficient, and resettlement issues were identified with the grouted connection (Mehmanparast et al., 2020) (J ö rss Blunck Ordemann, 2021). These technologies are called monopile to transition piece technologies (MP-TP).

The first offshore wind turbine installed in 1991 was 54 m high and 0.4 MW of power, while nowadays the new generation of wind turbines are 260 m high and 12 MW of power generation (Orsted, 2021). Wind turbines have now reached such a scale that large numbers of very large bolts, up to M90, are now commonly required in the MP-TP connections (Braithwaite and Mehmanparast, 2019), (Redondo and Mehmanparast, 2020), (Braithwaite et al., 2020). This has caused handling issues due to the sheer size of the bolts, problems due to the lack of standardisation, and reduced fatigue life due to a mixture of size and notch effects (Vanden Haute and Pire, 2020), (Lochan et al., 2019). Therefore, new MP-TP designs are emerging in the offshore wind market (Delwiche and Tavares, 2017). As mentioned previously, monopile foundations make up the vast majority of foundations in offshore wind turbines, and the offshore wind industry continues to grow dramatically. Therefore, the optimal performance of the MP-TP connection has a significant real-world impact and the introduction of an innovative MP-TP technology can noticeably reduce the LCOE in the new generation of offshore wind turbines.

1.3. The C1 wedge connection ™ technology

The wedge connection is a new type of MP-TP connection technology being developed by C1 Connections. As schematically demonstrated in Fig. 1, the core of this design is two wedges with inclined planes placed between two blocks, forming a wedge assembly. Using this technology, a
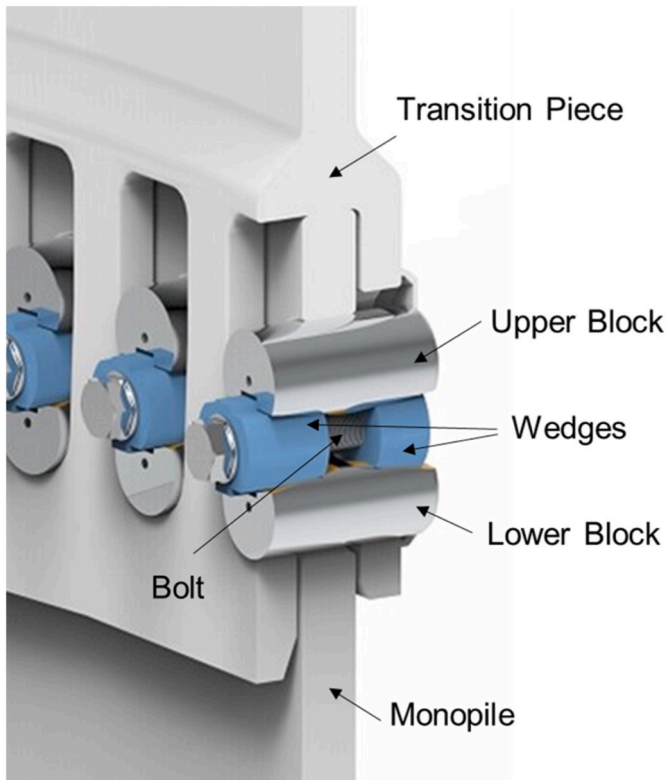
Fig. 1. C1 Connections wedge concept (Wind Innovators, 2021).

large number of these wedge assemblies are placed around the circumference of the MP-TP connection. As shown in Fig. 1, holes are also machined into the top section of the monopile to accommodate the wedge assemblies which effectively lock the transition piece into the monopile. During installation, the transition piece is placed on top of the monopile and the holes and wedge assemblies are aligned. The wedges are displaced horizontally, using a lateral bolt, with a hydraulic system. The hydraulic pressure is converted into a vertical preload through the inclined plane (Creusen, 2017), (Creusen et al., 2022). The wedge connection has a number of advantages, being easy to install and requiring little to no maintenance, according to the manufacturer (Wind Innovators, 2021). The design is intended to have a much higher load capacity and significantly better fatigue resistance than conventional flanged connections (Wind Innovators, 2021).

This paper aims to optimise the design of the wedge connection. This will include finding a lower bound on the preloading force required, considering whether the connection should be self-locking, and finding the optimal number of connections in one structure. The differences in Stress Concentration Factor (SCF) between a single wedge connection that may be used in laboratory tests and in the full structure will also be explored. Primarily analytical techniques will be used in this study, supported by Finite Element Modelling (FEM). In the modern day the default approach to many engineering problems is to deploy numerical techniques. Given the advances in FEM software in recent decades this is generally appropriate; however, the benefits of utilising analytical techniques should not be forgotten. A greater understanding of the problem can be gained by deploying such techniques, and they do not require extensive computational time. Often a combination of analytical and numerical approaches can be highly beneficial, as the two different techniques can be used to validate one another.

2. Finite element model

2.1. Model set-up

To support and compare against the analytical analysis, FEM analysis has been undertaken. One single wedge assembly segment, connecting the transition piece to the monopile, was considered. This assembly represents the structure likely to be used in any structural integrity experiments conducted in a laboratory setting. The finite element model consisted of one portion of the transition piece and the monopile, two blocks and two wedge components, as shown in Fig. 2. The bolts, nuts and washers were not considered for simplicity. The wedges were attached precisely to the blocks and then inserted into the hole formed by the monopile and the transition piece. The monopile and transition piece segments were built by assigning S460NL steel properties to them and the rest of the components were built with the 34CrNiMo6 alloy steel. The elastic properties of S460NL, which were derived from tensile tests, are summarised in Table 1 while the plastic deformation behaviour of the material is shown in Fig. 3. Also included in Table 1 are the elastic properties of 34CrNiMo6. It's worth noting that the tensile tests were carried out on specimens with 50 mm and 80 mm thickness, to account for the thickness effect in the thinner part (i.e. fork section of the transition piece) and thicker part (monopile section) of the geometry.

2.2. Mesh sensitivity analysis

In order to identify the most likely location of failure, a preliminary simulation was carried out with a coarse mesh. The result showed two primary hot zones in the monopile segment, Sections A and B (Fig. 4). Section B was very small and close to the edge, and its high stress value was mainly due to compression which is thought to have been caused by
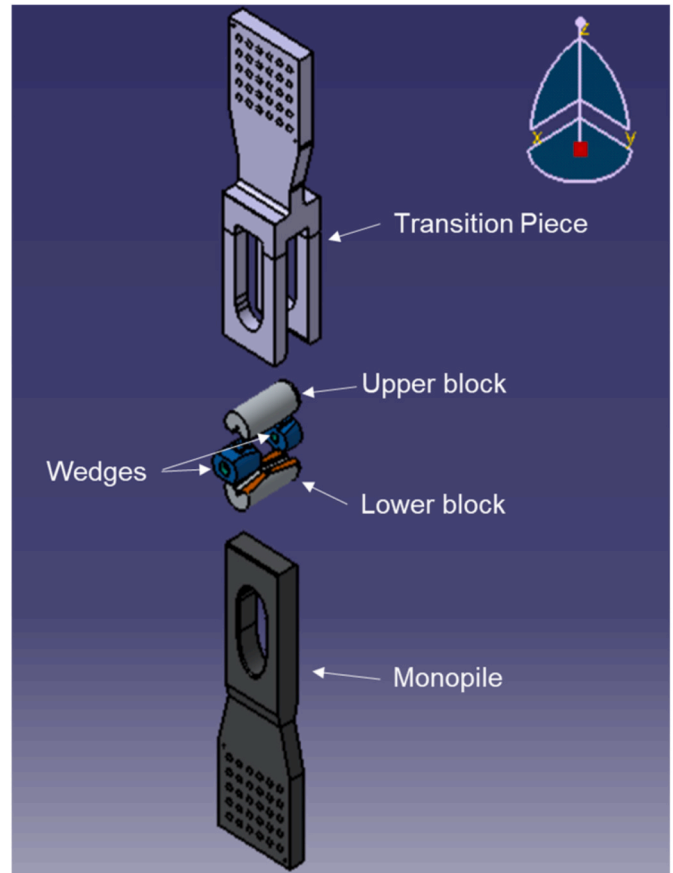

Fig. 2. Components of the finite element model.

Table 1

Elastic properties of S460NL and 34CrNiMo6.

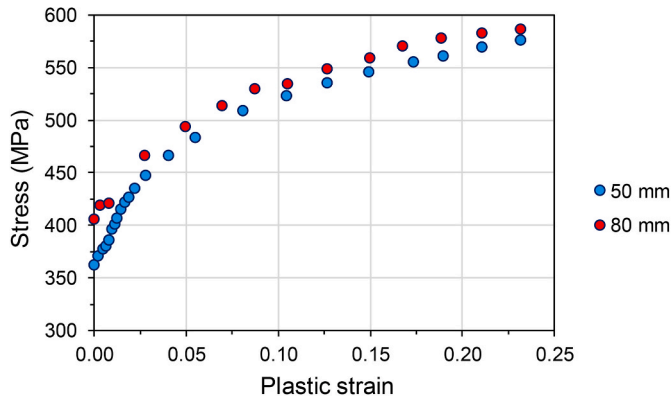| Material	S460NL	34CrNiMo6
Elastic Young's modulus (GPa)	212	205
Poisson's ratio	0.3	0.3
Density (Tonne/mm^3)	7.8×10^{-9}	7.73×10^{-9}

Fig. 3. S460NL plastic behaviour obtained from tensile specimens with 50 mm and 80 mm thickness.
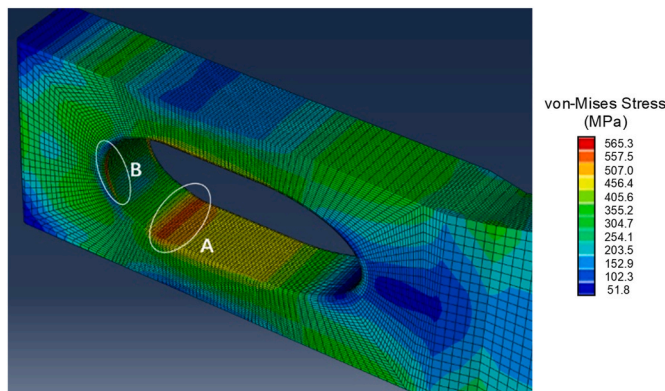

Fig. 4. High stress zones in the monopile segment.

the geometry of the model and the fillet design at the edges. For this this reason, Section A (which is located on both sides of the lower part of the fork section in the transition piece segment) was considered to be the most likely area of failure during the lifetime of a wedge connection. Thus, Section A had been selected, as the critical region for fatigue analysis, in the FEM process.

In order to find a more accurate critical region of the sample, the model was partitioned into smaller parts. Then, the mesh sensitivity test was concentrated in the critical region. Due to the fact that the block part has little influence on the result of critical zone and the geometry is complex and irregular, the mesh strategy for the block was quadratic tetrahedral. The element type used for this part in the simulation was C3D10M. Unlike the block component, the rest of the geometry was meshed by C3D8R hexagonal elements. By applying this kind of mesh strategy, the distortion of the elements is reduced, and a more accurate result is achieved. Also, to simplify the simulation process for mesh sensitivity analysis, the model was built with pure elasticity. This did not affect the accuracy of the results for mesh sensitivity analysis. By adjusting the element size of the critical region from 76,956 to 236,698, the maximum stress converged to 549.8 MPa when the element number in the critical region reached 195,888. The model which first reached the convergence plateau (see Fig. 5) was used for further analysis to save computing capacity as well as to ensure accurate results are obtained from FEM analysis. Upon completion of the mesh sensitivity analysis and identification of the optimum element size, plastic properties were also included in subsequent simulations performed in this study.

3. Spring system analysis

In this section, the wedge connection will be modelled analytically as a system of springs. This will allow for an estimation of the preload force, the displacement of the components with the system under preload and under external force, and the member forces on each component. Some insight into how preloading effects the system will be gained in this manner, and some of the other factors that affect the member forces on the components. The spring system will also allow for an estimation of a lower bound of the preload force that will ensure the connection does not loosen.

3.1. Spring model set-up

The system's initial state is considered to be the case where the wedges are at distance *l* from the end of the flat centre of the blocks, as
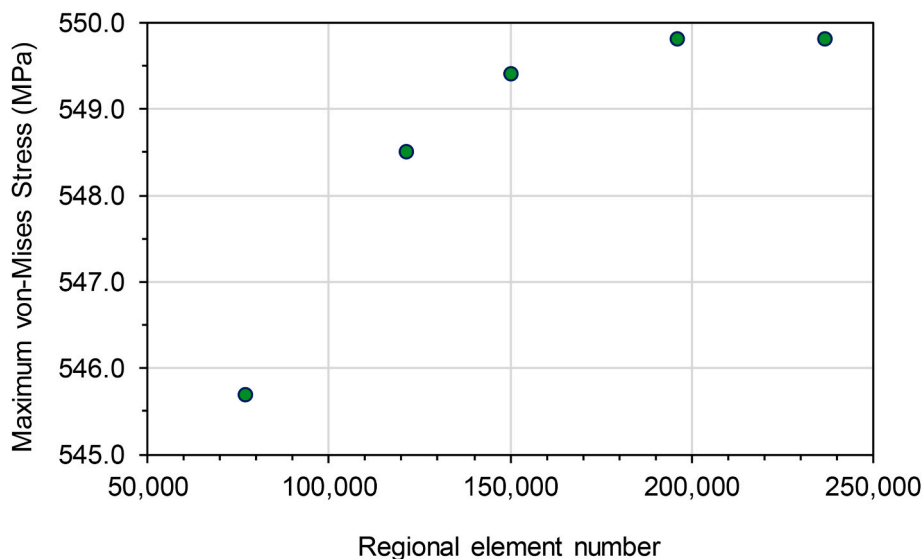

Fig. 5. The convergence curve of the mesh sensitivity analysis.

shown in Fig. 6(a), such that the wedges are in contact with both the upper and lower blocks but are not compressed; hence, every component is at its natural length. The natural length state of the system for the assembly is estimated based on the current wedge connection design. It should be noted however that this natural length state will be different in the full structure as the weight of the turbine on top of the connection will apply a force to the system and affect the starting positions of the components. It is first noted that the length of the through thickness lateral hole at the intersection point between the transition piece and the monopile is 226 *mm*, as shown in Fig. 6(b). The natural length of the shorter edge of the wedge is 58.8 *mm* (see Fig. 6(c)). The width of the blocks at their centre point is 82.3 *m*, meaning that the shortest distance between the upper and lower blocks is 55.5 *mm* (see Fig. 6(d)). Therefore, by considering Fig. 6(d), the length *l* can be found to be 11.9*mm*.

When the wedges are moved inwards from the natural length state by some distance x_0 then this can be viewed as the natural length of the wedge increasing by $2y_0$, where $y_0 = x_0 \tan(\alpha)$ and α is the angle that the wedge makes with the horizontal plane, as shown in Fig. 7. In the current wedge connection design, $\alpha = 8°$. The wedges are assumed to be inserted to a distance of 5.4 *mm* from the edge of the flat centre of the blocks, which is $x_0 = 11.9 - 5.4 = 6.5$ *mm* from the natural length state. Therefore, $y_0 = 6.5 \cdot \tan(8) = 0.914$ *mm*. It is worth noting that in practice, x_0 is a function of the preload applied to the bolt and the friction coefficient in the connection. Therefore, while a simplified assumption has been made in this study for the ease of mathematical calculations, the dependency of x_0 on preload and friction coefficient must be accounted for in case-specific industrial applications to achieve accurate solutions.

A single wedge connection can now be considered as a system of springs. As the system is reasonably symmetrical, the two wedges are considered as one spring, which means that the spring coefficient of the spring will be twice that of the coefficients of the individual wedges. Similarly, the relevant sections of the transition piece will be treated as one spring. The monopile is split into two springs in series, the section above the hole, denoted MP1, and the rest of the monopile, denoted MP2, as shown in Fig. 8. The portions of the transition piece considered are the sections parallel to the hole in the transition piece. This is treated as one spring and denoted TP. The upper and lower blocks are treated as two springs and denoted B1 and B2, respectively. As mentioned, the wedges are treated as one spring, denoted W. These components are all shown in Fig. 9. Let $C = \{MP1, MP2, TP, B1, B2, W\}$ denote the set of springs in the system.

In the natural length state, the spring system is as shown in Fig. 10. After the wedges have been moved inwards by x_0, the spring system moves to the configuration shown in Fig. 11. The variables $x_1, ..., x_7$ denote the distances moved from the first configuration to the second by the various nodes. The bottom of the monopile is treated as fixed.

3.2. FEM calculations of spring constants

The spring constant of each spring $i \in C$ is denoted K_i. Spring constants depend on the elastic Young's modulus of the material and the
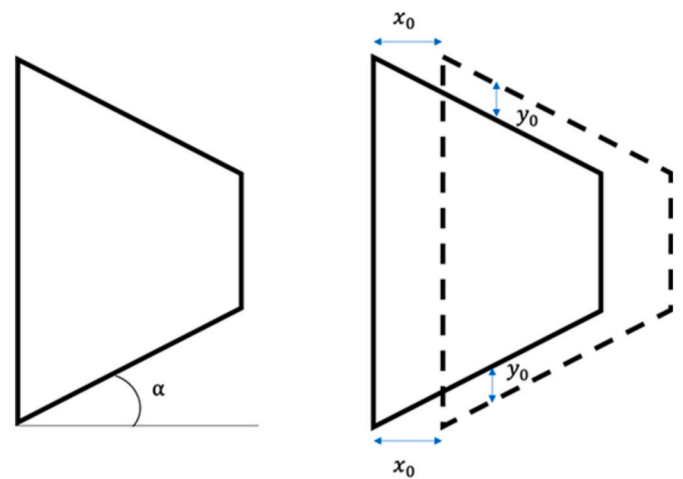

Fig. 7. Diagram of wedge parameters and relevant movements in vertical and horizontal directions.
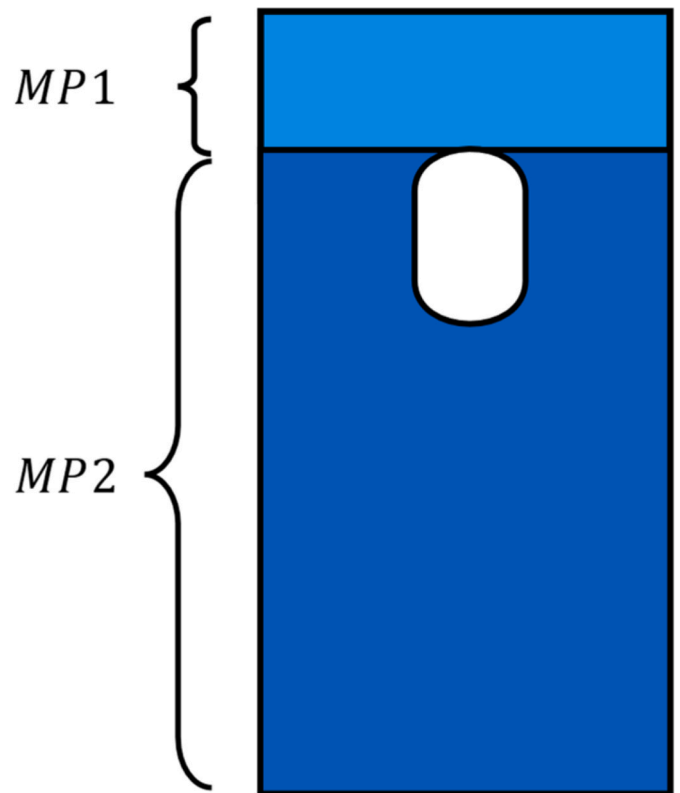

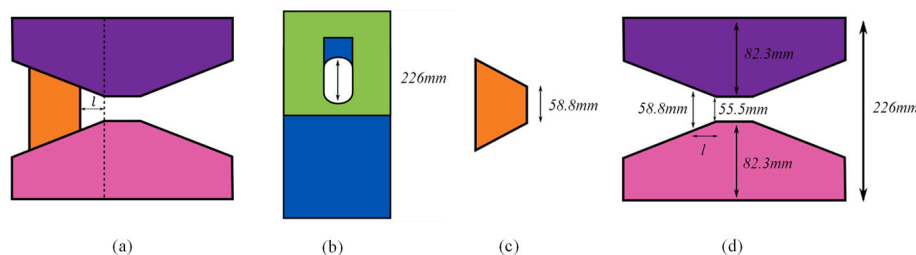**Fig. 8.** Monopile split into two springs, MP1 and MP2.

Fig. 6. Configuration of the wedges and the blocks (a) the wedges being a distance *l* from the end of the flat centre of the blocks, (b) dimension of the hole at the intersection point between the monopile and transition piece, (c) dimension of the wedges, (d) dimensions of the upper and lower blocks in the current wedge connection design.
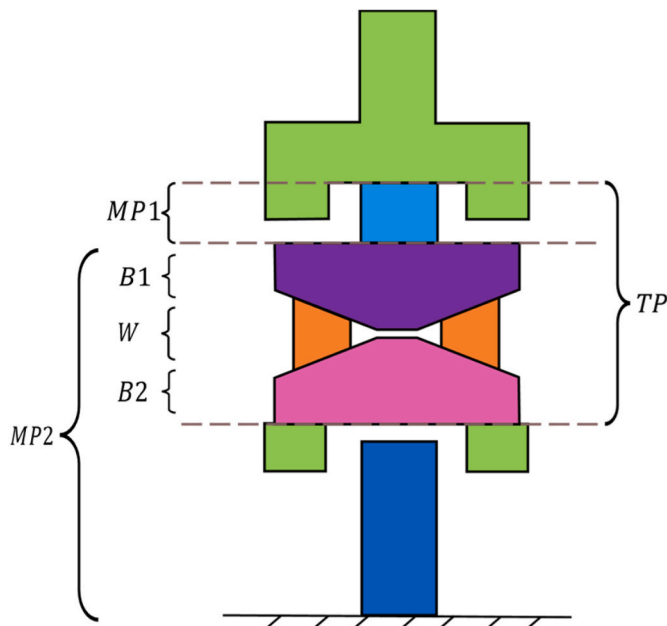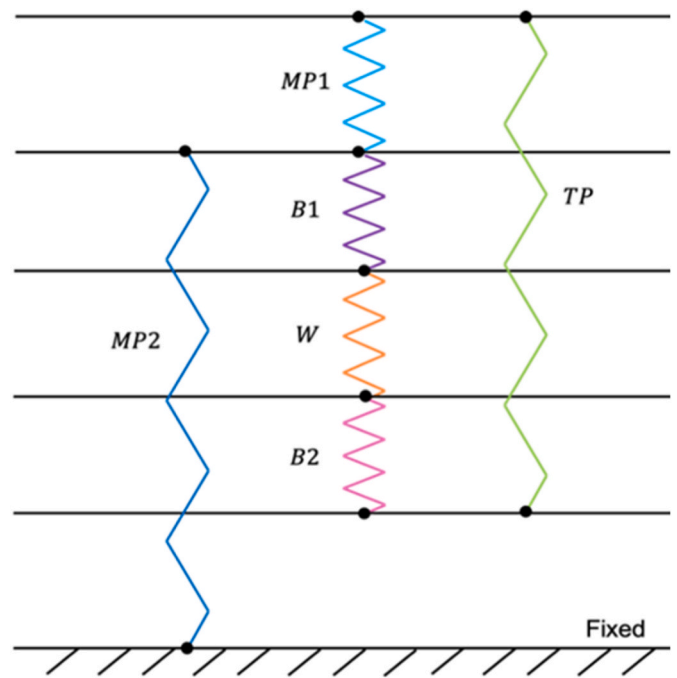
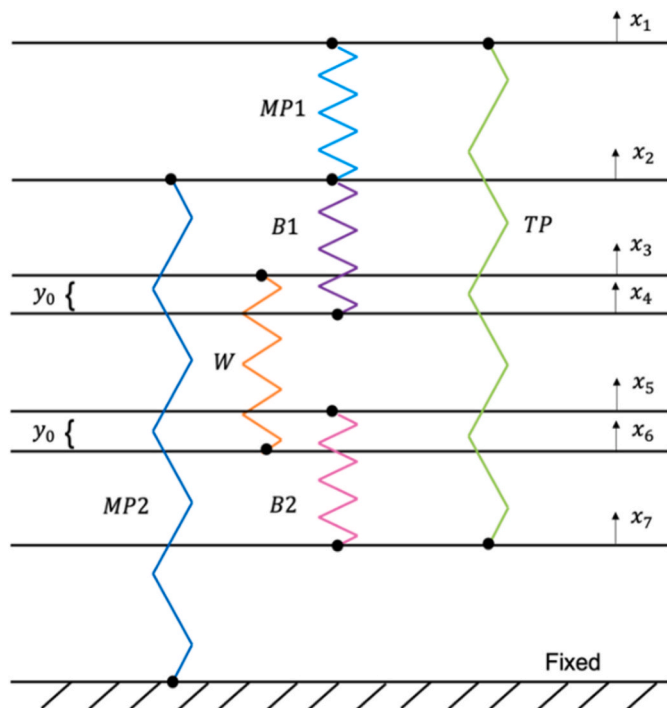**Fig. 9.** Components of the spring system.

Fig. 10. Spring system in natural length state.

geometry of the spring. Due to the complexity of the geometries in this system, calculating these values analytically is extremely difficult. Therefore, these values have been estimated via FEM analysis. This is detailed in Appendix A. In order to evaluate the spring constants in FEM simulations, a uniaxial segment with a single wedge connection which was designed for experimental investigations was considered in the analysis. This explains the reason why K_{B1} and K_{B2} were assumed to be the same in the present study. While this assumption is valid for a simplified laboratory-based segment analysis, case-specific values need to be defined for each of these spring constants based on the design criteria and the operational loading conditions that may impose deferent

Fig. 11. Spring system after insertion of wedges.

degrees of bending on B1 and B2. To calculate K_{MP2}, the length of the monopile considered in the analysis was assumed as 25m. It should be noted that the meshing on the blocks and the wedges was primarily aimed at optimising the accuracy of the results on the transition piece in the FEM analysis, hence the spring constants are considered to be approximations. The same methodology could be applied with an improved meshing strategy to increase the reliability of the spring constant values. The spring constant results are summarised in Table 2.

3.3. Preloading

The system described in Section 3.1 is now solved, which will provide the node displacements, the spring deformations, the member forces, and the preloading in the system. The following analysis follows a similar process to the one described in Reference (Crescimanno and Keller, 1981), although an energy approach is taken as opposed to resolving of forces (Goodman and Warner, 1963). Let δ_i denote the expansion (or compression) of spring $i \in C$, which can be written in terms of the displacement of nodes as shown in Table 3.

Let IL_i, FL_i denote the initial and final lengths of component $i \in C$, respectively. Then:

$$IL_{TP} = IL_{MP1} + IL_{B1} + IL_{B2} + IL_W - 2y_0 \qquad \text{Equation(1)}$$

$$FL_{TP} = FL_{MP1} + FL_{B1} + FL_{B2} + FL_W \qquad \text{Equation(2)}$$

Hence:

Table 2
Spring constants derived via FEM.

Spring	Spring Constant (MN/mm)
K_{MP1}	4.00
K_{B1}, K_{B2}	18.9
K_{TP}	2.07
K_{MP2}	0.14
K_W	19.7

Table 3
Expansion or compression of springs $i \in C$ in terms of the displacement of nodes.

The expansion (or compression) of spring $i \in C$	Expression in terms of displacement of nodes
δ_{TP}	$x_1 - x_7$
δ_{MP1}	$x_1 - x_2$
δ_{B1}	$x_2 - x_4$
δ_{B2}	$x_5 - x_7$
δ_W	$x_3 - x_6$
δ_{MP2}	x_2

$$(FL_{TP} - IL_{TP}) = (FL_{MP1} - IL_{MP1}) + (FL_{B1} - IL_{B1}) + (FL_{B2} - IL_{B2}) \\ + (FL_W - IL_W) + 2y_0 \tag{Equation(3)}$$

$$\delta_{TP} = \delta_{MP1} + \delta_{B1} + \delta_{B2} + \delta_W + 2y_0 \tag{Equation(4)}$$

$$x_1 = x_1 - x_2 + x_2 - x_4 + x_5 + x_3 - x_6 + 2y_0 \tag{Equation(5)}$$

$$x_3 - x_6 = x_4 - x_5 - 2y_0 \tag{Equation(6)}$$

Then the energy of the system is:

$$E = \frac{K_{MP1}}{2}(x_1 - x_2)^2 + \frac{K_{B1}}{2}(x_2 - x_4)^2 \frac{K_W}{2}(x_3 - x_6)^2 + \frac{K_{B2}}{2}(x_5 - x_7)^2 \\ + \frac{K_{TP}}{2}(x_1 - x_7)^2 + \frac{K_{MP2}}{2}x_2^2 \tag{Equation(7)}$$

Subbing in Equation (6)) gives:

$$E = \frac{K_{MP1}}{2}(x_1 - x_2)^2 + \frac{K_{B1}}{2}(x_2 - x_4)^2 \frac{K_W}{2}(x_4 - x_5 - 2y_0)^2 + \frac{K_{B2}}{2}(x_5 - x_7)^2 \\ + \frac{K_{TP}}{2}(x_1 - x_7)^2 + \frac{K_{MP2}}{2}x_2^2 \tag{Equation(8)}$$

The energy of the system must be minimised. Hence, the partial differential of the energy with respect to each variable must be zero. This gives the following system of linear equations:

$$\begin{pmatrix} K_{MP1} + K_{TP} & -K_{MP1} & 0 & 0 & -K_{TP} \\ -K_{MP1} & K_{MP1} + K_{B1} + K_{MP2} & -K_{B1} & 0 & 0 \\ 0 & -K_{B1} & K_{B1} + K_W & -K_W & 0 \\ 0 & 0 & -K_W & K_W + K_{B2} & -K_{B2} \\ -K_{TP} & 0 & 0 & -K_{B2} & K_{B2} + K_{TP} \end{pmatrix} \begin{pmatrix} x_1 \\ x_2 \\ x_4 \\ x_5 \\ x_7 \end{pmatrix} = \begin{pmatrix} 0 \\ 0 \\ 2K_W y_0 \\ -K_W y_0 \\ 0 \end{pmatrix} \tag{Equation(9)}$$

Subsequently, the following K domain is defined:

$$K_{DOM} = \sum_{i \in C \backslash \{MP2\}} \frac{1}{K_i} = \frac{1}{K_{B1}} + \frac{1}{K_{B2}} + \frac{1}{K_W} + \frac{1}{K_{MP1}} + \frac{1}{K_{TP}} \tag{Equation(10)}$$

From the spring constant estimates, K_{DOM} can be estimated as:

$$K_{DOM} = \frac{1}{18.9} + \frac{1}{18.9} + \frac{1}{19.7} + \frac{1}{4.00} + \frac{1}{2.07} = 0.887 \; mm \Big/ MN \tag{Equation(11)}$$

Solving the system of linear equations gives Table 4.
And since $x_3 - x_6 = x_4 - x_5 - 2y_0$,

$$x_3 - x_6 = \frac{2y_0 \left(\frac{1}{K_{B1}}\right)}{K_{DOM}} - \frac{-2y_0 \left(\frac{1}{K_{TP}} + \frac{1}{K_{MP1}} + \frac{1}{K_{B2}}\right)}{K_{DOM}} - 2y_0 \tag{Equation(12)}$$

Table 4
Solution to node displacements in preloaded system.

Node displacement	Solution
x_1	$\dfrac{-2y_0 \frac{1}{K_{MP1}}}{K_{DOM}}$
x_2	0
x_4	$\dfrac{2y_0 \left(\frac{1}{K_{B1}}\right)}{K_{DOM}}$
x_5	$\dfrac{-2y_0 \left(\frac{1}{K_{TP}} + \frac{1}{K_{MP1}} + \frac{1}{K_{B2}}\right)}{K_{DOM}}$
x_7	$\dfrac{-2y_0 \left(\frac{1}{K_{TP}} + \frac{1}{K_{MP1}}\right)}{K_{DOM}}$

$$x_3 - x_6 = \frac{2y_0 \left(\frac{1}{K_{TP}} + \frac{1}{K_{MP1}} + \frac{1}{K_{B1}} + \frac{1}{K_{B2}}\right)}{K_{DOM}} - \frac{2y_0 K_{DOM}}{K_{DOM}} \tag{Equation(13)}$$

$$x_3 - x_6 = \frac{-2y_0 \frac{1}{K_W}}{K_{DOM}} \tag{Equation(14)}$$

Therefore, the solution to the change in lengths of the springs and evaluation at $x_0 = 6.5 \; mm$ are given in Table 5.
Therefore, for all $i \in C \backslash \{MP2\}$,

$$|\delta_i| = \frac{2y_0 \frac{1}{K_i}}{K_{DOM}} \tag{Equation(15)}$$

And so, the size of the member force of spring $i \in C \backslash \{MP2\}$ is:

$$|F_i| = |\delta_i| K_i = \frac{2y_0}{K_{DOM}} = \frac{2x_0 \tan(\alpha)}{K_{DOM}} \tag{Equation(16)}$$

Therefore, the preload, PL, is:

$$PL = \frac{2x_0 \tan(\alpha)}{K_{DOM}} \tag{Equation(17)}$$

Which can be estimated via the spring constants as:

Table 5
Solution to spring compressions in preloaded system.

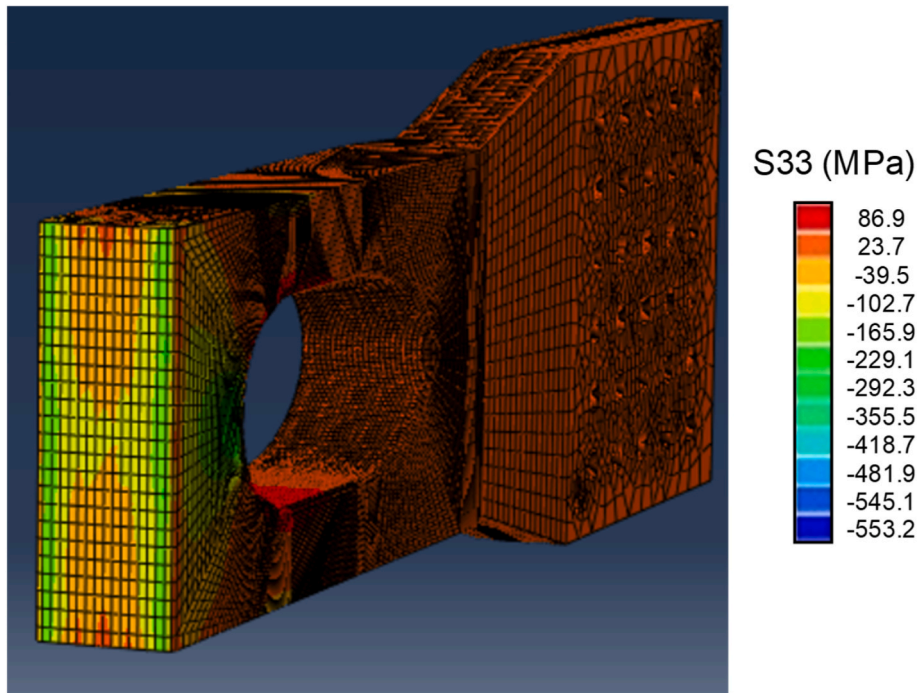| Spring compression (or expansion)	Solution	Evaluation at $x_0 = 6.5 \; mm$
δ_{TP}	$\dfrac{2y_0 \frac{1}{K_{TP}}}{K_{DOM}}$	$\dfrac{2 \cdot 0.914 \cdot \frac{1}{2.07}}{0.887} = 0.995 \; mm$
δ_{MP1}	$\dfrac{-2y_0 \frac{1}{K_{MP1}}}{K_{DOM}}$	$\dfrac{2 \cdot 0.914 \cdot \frac{1}{4.00}}{0.887} = 0.515 \; mm$
δ_{B1}	$\dfrac{-2y_0 \frac{1}{K_{B1}}}{K_{DOM}}$	$\dfrac{2 \cdot 0.914 \cdot \frac{1}{18.9}}{0.887} = 0.109 \; mm$
δ_{B2}	$\dfrac{-2y_0 \frac{1}{K_{B2}}}{K_{DOM}}$	$\dfrac{2 \cdot 0.914 \cdot \frac{1}{18.9}}{0.887} = 0.109 \; mm$
δ_W	$\dfrac{-2y_0 \frac{1}{K_W}}{K_{DOM}}$	$\dfrac{2 \cdot 0.914 \cdot \frac{1}{19.7}}{0.887} = 0.105 \; mm$
δ_{MP2}	$0 \; mm$	$0 \; mm$

Fig. 12. Preload contact stress (S33).

$$PL = \frac{2 \cdot 6.5 \cdot \tan(8)}{0.887} = 2.06 \, MN \qquad \text{Equation(18)}$$

The preload was also calculated via FEM analysis, as shown in Fig. 12. The total contact force at the surface was found to be 2.13 MN, a 2.28% difference with the analytical solution. Given the simplifications associated with the analytical model, this degree of difference is small and supports the analytical model.

As the natural length state has been calculated, it must be that $0 \leq x_0 \leq 11.9mm$, and so an upper bound on the possible preload can be estimated as:

$$\frac{2 \cdot 11.9 \cdot \tan(8)}{0.887} = 3.77 \, MN \qquad \text{Equation(19)}$$

It should be noted that since $\delta_{MP2} = x_2 = 0$, the monopile below the top of the holes is not deformed and does not take any preload force.

3.4. Energy required for preloading

Now the forces acting on one of the wedges are considered, as shown in Fig. 13. In this figure, F_P is the force applied by the lateral bolt, F_U is the force exerted on the wedge by the upper block, F_L is the force from the lower block, the friction force from the upper block is denoted f_U and f_L is the friction force from the lower block. The friction coefficient between the blocks and the wedges is denoted μ. In the current design, μ is assumed to be 0.06. So, whilst the preload is being applied, the frictional forces will be maximal and so $f_U = \mu F_U$ and $f_L = \mu F_L$.

Using the adiabatic approximation (Handy and Lee, 1996), it can be assumed that the system is always in equilibrium. Therefore, resolving the horizontal forces gives:

$$F_P - \mu F_U \cos(\alpha) - \mu F_L \cos(\alpha) - F_U \sin(\alpha) - F_L \sin(\alpha) = 0 \qquad \text{Equation(20)}$$

Since the forces will depend on the distance x that the wedge has been pushed inwards from the start position, F_P, F_U and F_L are functions of x:

$$F_P(x) = (F_U(x) + F_L(x))(\mu \cos(\alpha) + \sin(\alpha)) \qquad \text{Equation(21)}$$

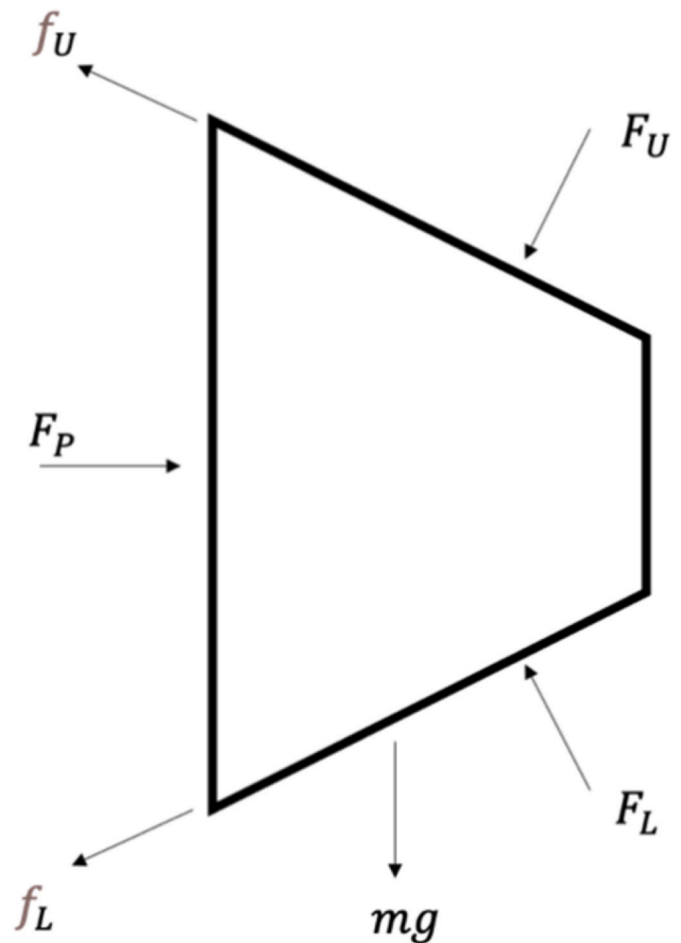$F_U(x)$ and $F_L(x)$ can be calculated from the work done to calculate the

Fig. 13. Free-body diagram of wedge.

preload (PL) in the system. Mass forces are neglected as they are either already captured in the starting position of the equilibrium, or they are negligible. Resolving the forces on the upper (or lower) block therefore gives that:

$$F_U(x) = F_L(x) = \frac{PL}{2}\cos(\alpha) = \frac{2x\tan(\alpha)}{2K_{DOM}}\cos(\alpha) = \frac{x\sin(\alpha)}{K_{DOM}} \qquad \text{Equation(22)}$$

Therefore:

$$F_P(x) = \frac{2x\sin(\alpha)}{K_{DOM}}(\mu\cos(\alpha) + \sin(\alpha)) \qquad \text{Equation(23)}$$

So, the energy required to move both wedges in by a distance x_0 can be calculated via the following integral:

$$rgy = \int_0^{x_0} 2F_P(x)dx = \int_0^{x_0} 2\frac{2x\sin(\alpha)}{K_{DOM}}(\mu\cos(\alpha) + \sin(\alpha))dx$$

$$= \frac{2x_0^2\sin(\alpha)}{K_{DOM}}(\mu\cos(\alpha) + \sin(\alpha))$$

$$\text{Equation(24)}$$

Which, in the case where $x_0 = 6.5\,mm$, can be evaluated as the following for the current design:

$$\frac{2\cdot 6.5^2\sin 8}{0.887}(0.06\cos(8) + \sin(8)) = 2.63\,MNmm = 2,633\,J \qquad \text{Equation(25)}$$

Recall that the energy stored in the spring system after having moved the wedges inwards by x_0 is the following, which can also be evaluated for the current design:

$$\sum_{i\in C}\frac{K_i}{2}\delta_i^2 = \sum_{i\in C}\frac{K_i}{2}\left(\frac{2x_0\tan(\alpha)\frac{1}{K_i}}{K_{DOM}}\right)^2 = \frac{2x_0^2\tan(\alpha)^2}{K_{DOM}^2}\sum_{i\in C}\frac{1}{K_i} = \frac{2x_0^2\tan(\alpha)^2}{K_{DOM}}$$

$$= 1.88\,MNmm = 1,882\,J$$

$$\text{Equation(26)}$$

Therefore, the energy lost to friction when moving the wedges
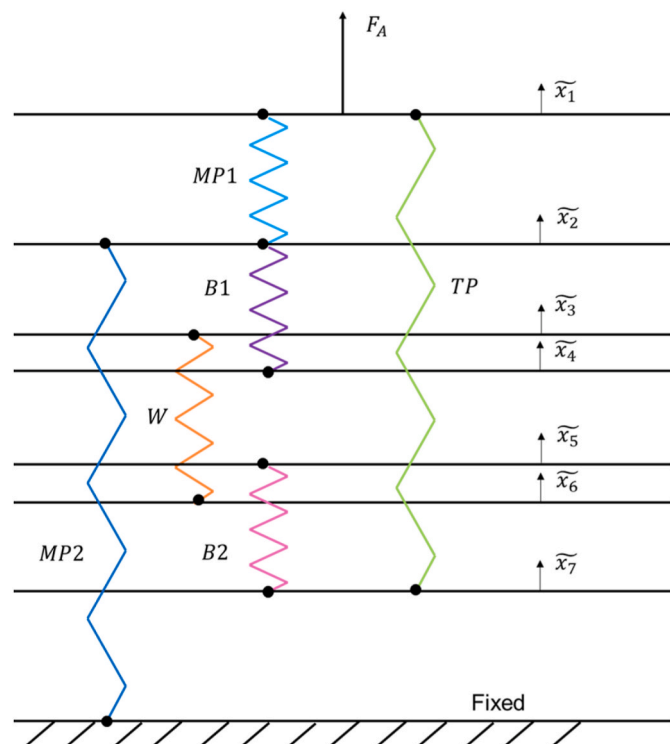

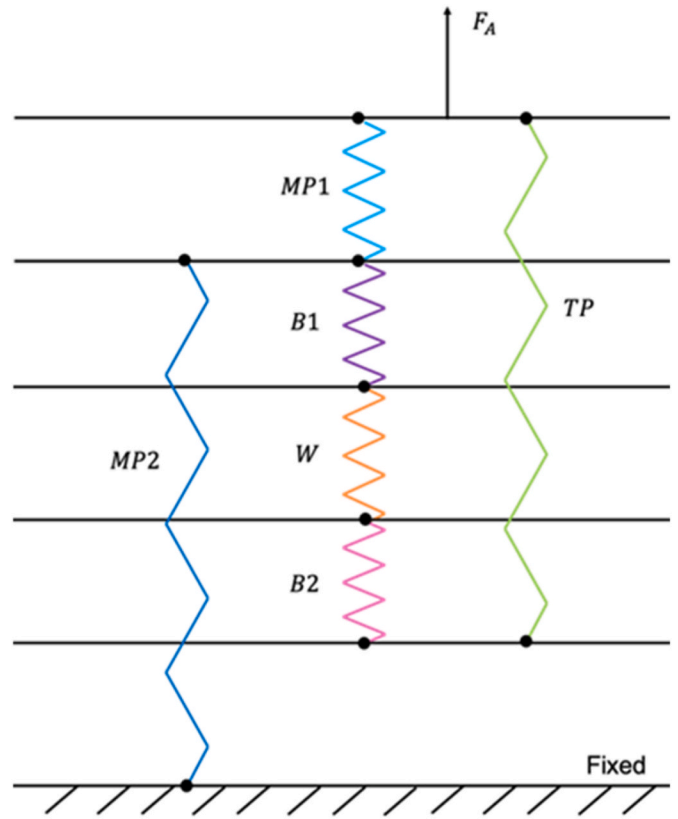**Fig. 14.** Spring system in natural length state.

Fig. 15. Spring system after insertion of wedges and with application of axial force.

Table 6
Solution to spring compressions in preloaded system with externally applied axial force.

pring compression (or expansion)	Solution	Evaluation at $F_A = 2.3\,MN$ and $x_0 = 6.5\,mm$
$\widetilde{\delta}_{MP1}$	$\frac{1}{K_{MP1}}\left(F_A - \frac{F_A}{K_{DOM}K_{MP1}} - PL\right)$	$-0.102\,mm$
$\widetilde{\delta}_{TP}$	$\frac{1}{K_{TP}}\left(\frac{F_A}{K_{MP1}K_{DOM}} + PL\right)$	$1.30\,mm$
$\widetilde{\delta}_{B1}$	$-\frac{1}{K_{B1}}\left(\frac{F_A}{K_{MP1}K_{DOM}} + PL\right)$	$-0.143\,mm$
$\widetilde{\delta}_{B2}$	$-\frac{1}{K_{B2}}\left(\frac{F_A}{K_{MP1}K_{DOM}} + PL\right)$	$-0.143\,mm$
$\widetilde{\delta}_W$	$-\frac{1}{K_W}\left(\frac{F_A}{K_{MP1}K_{DOM}} + PL\right)$	$0.137\,mm$
$\widetilde{\delta}_{MP2}$	$\frac{F_A}{K_{MP2}}$	$16.4\,mm$

inwards by x_0 is:

$$\frac{2x_0^2\sin(\alpha)}{K_{DOM}}(\mu\cos(\alpha) + \sin(\alpha)) - \frac{2x_0^2\tan(\alpha)^2}{K_{DOM}}$$

$$= \frac{2x_0^2}{K_{DOM}}\left(\sin(\alpha)\left((\mu\cos(\alpha) + \sin(\alpha)) - \tan(\alpha)^2\right)\right) = 751\,J$$

$$\text{Equation(27)}$$

However, it should be noted that Equation (24) is a lower bound on

Table 7
Comparison of the analytical and FEM solutions for the spring deformations after preloading and application of 2.3 MN force.

Spring compression (or expansion)	Analytical Solution	FEM solution
$\widetilde{\delta}_{MP1}$	$-0.102\ mm$	$-0.129\ mm$
$\widetilde{\delta}_{TP}$	$1.30\ mm$	$0.829\ mm$
$\widetilde{\delta}_{B1}, \widetilde{\delta}_{B2}$	$-0.143\ mm$	$-0.011\ mm$
$\widetilde{\delta}_{W}$	$0.137\ mm$	$0.207\ mm$

the energy required to pull the wedges together. This is because an idealised model has been used that doesn't take into account other forms of energy loss during tensioning.

3.5. External axial force

Now the application of an external force to the system is considered. Let F_A be an axial force applied to the system, as shown in Figs. 14 and 15. Let $\widetilde{x}_1, ..., \widetilde{x}_7$ denote the new distances moved by the various nodes, as shown in Fig. 14.

Let $\widetilde{\delta}_i$ denote the new expansion (or compression) of spring $i \in C$. The general solution to the system is provided in Table 6, alongside the evaluation for the case that $F_A = 2.3\ MN$ and $x_0 = 6.5\ mm$. The method used for this purpose has been explained in detail in Appendix B.

These results can be compared with the solution found using FEM. During this simulation, a load of 2.3 MN was applied at the top surface of the transition piece as an external load. The bottom of the monopile was fixed via a symmetry ENCASTRE boundary condition. Appendix B details how the spring deformations were extracted from the FEM. Table 7 compares the deformation results by the two methods. Recall that the solution for $\widetilde{\delta}_{MP2}$ assumes a spring constant associated with a full-scale 25m long monopile and hence cannot be directly compared with the FEM results which are based on a small-scale segment of the wedge connection. Considering the large dimensions of the MP-TP connection, the results are reasonably close (with less than 1 mm difference between analytical and FEM values) despite the simplification associated with the analytical model, including the fact that the analytical model assumes fully elastic deformation whereas the FEM result is based on elastic-plastic simulations.

Let $\widetilde{F}_i$ denote the member force of spring i $\in C$. Then $\widetilde{F}_i = \widetilde{\delta}_i K_i$, hence

$$\widetilde{F}_{MP2} = F_A \qquad \text{Equation(28)}$$

$$\widetilde{F}_{TP} = \frac{F_A}{K_{DOM}K_{MP1}} + PL \qquad \text{Equation(29)}$$

$$\widetilde{F}_{MP1} = F_A - \frac{F_A}{K_{DOM}K_{MP1}} - PL \qquad \text{Equation(30)}$$

And for $i = B1, B2$ and W:

$$\widetilde{F}_i = \frac{-F_A}{K_{DOM}K_{MP1}} - PL \qquad \text{Equation(31)}$$

In the case where $F_A = 2.3\ MN$ and $x_0 = 6.5\ mm$, we have that:

$$\widetilde{F}_{MP2} = 2.3\ MN \qquad \text{Equation(32)}$$

$$\widetilde{F}_{TP} = 2.7\ MN \qquad \text{Equation(33)}$$

$$\widetilde{F}_{MP1} = -0.409\ MN \qquad \text{Equation(34)}$$

And for $i = B1, B2$ and W:

$$\widetilde{F}_i = -2.7\ MN \qquad \text{Equation(35)}$$

So, the total externally applied axial force is applied to $MP2$. Recall the definition of K_{DOM} given in Equation (10). So $1/K_{DOM}$ is what the stiffness of a spring consisting of all springs $i \in C\backslash\{MP2\}$ in series would

be. Looking at the expressions for the member forces of the springs, the only way in which the stiffnesses of each individual spring affect these is through the term $K_{DOM}K_{MP1}$. This is the ratio of the stiffness of $MP1$ to a spring with stiffness $1/K_{DOM}$. Therefore, the ratio of the stiffness of any other springs in C will not affect the ratio of the member forces of the springs.

3.6. Force required to loosen connection

Recall that the calculated $\widetilde{\delta}_i$ are the compressions or expansions from the natural length state. In the case of the structure in situ, the mass of the transition piece and turbine are sat on top of the system and will affect the natural length state. So $\widetilde{\delta}_{MP1} = 0$ corresponds to MP1 being compressed by exactly the amount it would be from just the transition piece and turbine sitting on top of it. MP1 being fully uncompressed therefore in fact corresponds to approximately $\widetilde{\delta}_{MP1} = (mg/n)/K_{MP1}$ where m is the mass of the transition piece and the turbine, g is acceleration due to gravity and n is the number of connections. Hence, the tensile force required to lift the transition piece up off the monopile can be estimated:

$$\frac{mg}{n\ K_{MP1}} = \frac{1}{K_{MP1}}\left(F_A - \frac{F_A}{K_{DOM}K_{MP1}} - PL\right) \qquad \text{Equation(36)}$$

$$\frac{mg}{n} = F_A\left(1 - \frac{1}{K_{DOM}K_{MP1}}\right) - PL \qquad \text{Equation(37)}$$

$$F_A\left(\frac{K_{DOM}K_{MP1} - 1}{K_{DOM}K_{MP1}}\right) = \frac{mg}{n} + PL \qquad \text{Equation(38)}$$

$$F_A = \frac{\left(\frac{mg}{n} + PL\right)K_{DOM}K_{MP1}}{K_{DOM}K_{MP1} - 1} \qquad \text{Equation(39)}$$

This equation can be evaluated for any given offshore wind turbine. For example, for a structure like a V80–2.0, the mass of the wind turbine would be 230 tonnes (Bhattacharya, 2019), (Vestas, 2011). Assuming a diameter of 4m, a length of 20m and a wall thickness of 5 cm, the volume of the transition piece is estimated as $12.4\ m^3$ via the following equation:

$$Volume = Annulus\ area \times length\ of\ cylinder = \left(\pi R^2 - \pi(R - w)^2\right) \times L$$
$$\text{Equation(40)}$$

Assuming a density of 7.8 tonnes/m³ (OVAKO, 2021), this is 96.8 tonnes, hence it can assumed that $m = 326.8$ tonnes. The number of connections n is taken to be the optimal value estimated in Section 4.1 for a 4m diameter turbine with hole width 115 mm; which is 59. Therefore, the force required to loosen the connection can be estimated in this case as:

$$\frac{\left(\frac{326800\cdot 9.8}{59} + 2.06\cdot 10^6\right)\cdot 0.887\cdot 4.00}{0.887\cdot 4.00 - 1} = 2944000\ N = 2.9\ MN \qquad \text{Equation(41)}$$

Conversely, an estimation on the lower bound that the preload value should be set to can be expressed as the following:

$$PL \geq F_{A,max}\left(\frac{K_{DOM}K_{MP1} - 1}{K_{DOM}K_{MP1}}\right) - \frac{mg}{n} \qquad \text{Equation(42)}$$

where $F_{A,max}$ is the largest predicted tensile load. It is worth noting that in addition to the gravity-based analysis explained above, suitable safety factors must be considered to account for other self-loosing mechanisms such as vibration in the calculation of the minimum required preload that maintains the MP-TP connection using the wedge technology.

3.7. Bolts in the wedge connection

The SCF on the threads of bolts are high due to the notch effect. Bolts that are subjected to cyclic loading of large amplitudes and high
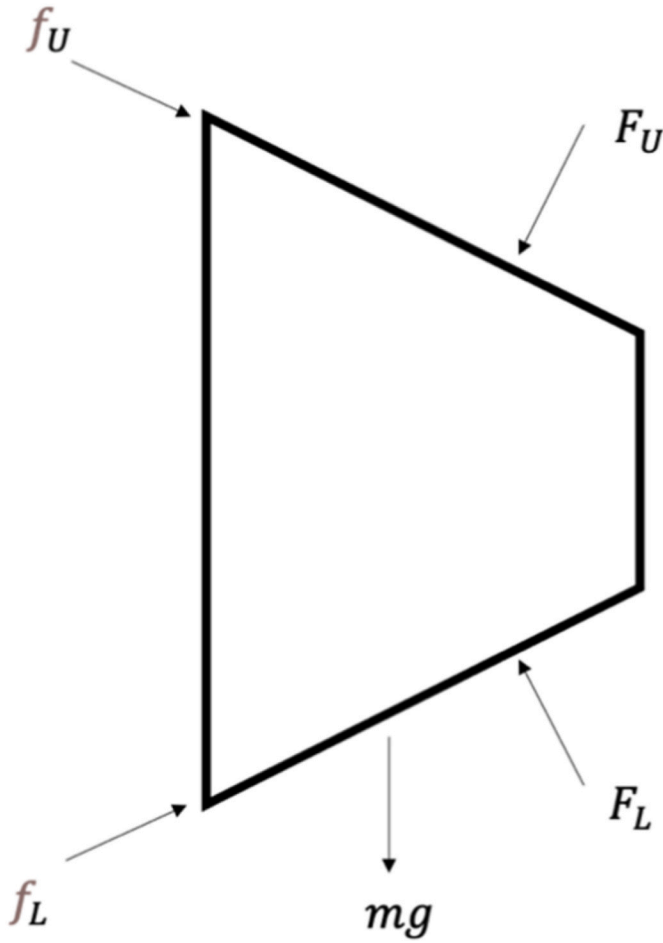
Fig. 16. Free-body diagram of wedge in case of broken bolt.

numbers of load cycles, such as those in MP-TP flanged bolted connections, are therefore vulnerable to fatigue failure (Schaumann and Eichstädt, 2015). In MP-TP flanged bolted connections, preloading is therefore very important as the preloaded compressed flange will take the majority of an external tensile load since the flange material is stiffer than the bolt (Richards, 2018). The wedge component also includes a bolt which is tightened to bring the two wedges closer together and apply a preload to the system. The parameters in this design can, in fact, be selected so as to ensure a self-locking mechanism. This would mean that, if the bolt fails, the frictional forces would hold the wedges in place and maintain the preloading throughout the system.

If the bolt fails, then the force F_P is no longer applied to the wedge, therefore, the only forces on the wedge in the inwards direction are the

horizontal components of the frictional forces f_U and f_L as can be seen in Fig. 16. To prevent the wedges from moving outwards, it is therefore necessary that:

$$(f_U + f_L)\cos \alpha \geq (F_U + F_L)\sin \alpha \qquad \text{Equation(43)}$$

$$\mu(F_U + F_L)\cos \alpha \geq (F_U + F_L)\sin \alpha \qquad \text{Equation(44)}$$

$$\mu \cos \alpha \geq \sin \alpha \qquad \text{Equation(45)}$$

$$\mu \geq \tan \alpha \qquad \text{Equation(46)}$$

Therefore, the angle α can be selected to ensure that $\tan \alpha$ remains less than the coefficient of friction between the wedge and the upper and lower blocks.

In the current design however, the friction coefficient between the blocks and the wedges is 0.06 and $\alpha = 8°$, so:

$$tan(\alpha) = 0.14 \not\leq 0.06 = \mu \qquad \text{Equation(47)}$$

The self-locking quality is only desirable however if failure of the bolts in the wedge connection is considered a reasonable possibility. By considering the diagram in Fig. 17, the tensile load on the bolt in the wedge connection can be calculated.

$$F_P = (F_U + F_L)\sin(\alpha) - (f_U + f_L)\cos(\alpha) \qquad \text{Equation(48)}$$

$$\geq (F_U + F_L)(\sin(\alpha) - \mu \cos(\alpha))$$

Recalling the solutions to the member forces on the springs in Section 3.5, and resolving the forces on the upper block, it can be seen that:

$$F_U = F_L = \left(\frac{F_A}{K_{DOM}K_{MP1}} + PL\right) \frac{\cos(\alpha)}{2} \qquad \text{Equation(49)}$$

And so, the varying portion of the force on the bolt in the connection, denoted $F_{P,V}$, has the following lower bound:

$$F_{P,V} \geq \left(\frac{F_A}{K_{DOM}K_{MP1}}\right)\cos(\alpha)(\sin(\alpha) - \mu \cos(\alpha))$$

$$= \left(\frac{F_A}{4.00 \cdot 10^{-6} \cdot 0.887 \cdot 10^6}\right)\cos(8)(\sin(8) - 0.06\cos(8)) = 0.022\, F_A$$

$$\text{Equation(50)}$$

Hence, a lower bound on the varying force on the bolt can be obtained. The preload effect on reducing the force taken by the bolt has been neglected, hence this lower bound is conservative. Since a small proportion of the tensile force on one connection is translated to the bolt in that connection, failure of the bolt is not considered likely. Therefore, the self-locking quality is not considered to be a required feature.
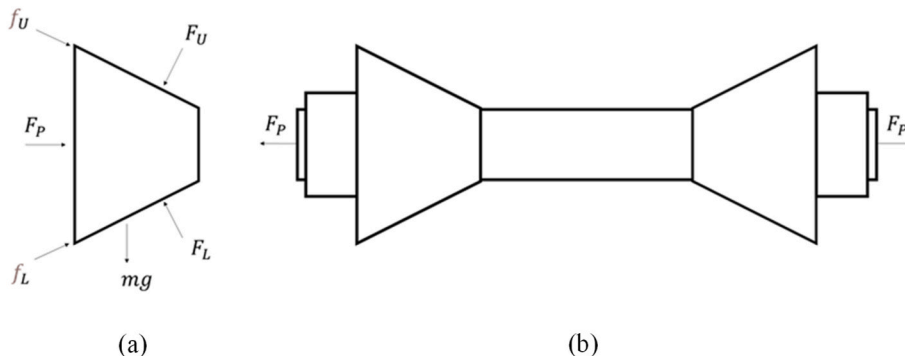

(a)   (b)

Fig. 17. (a) Free-boday diagram of wedge and (b) resulting tensile force on bolt.

4. Optimal number of connections and SCF

4.1. Optimal number of wedge connections

An important design question is the number of wedge connections that should attach the monopile to the transition piece. This can be determined by looking to minimise the stress concentration as a function of the number of connections. In the current design, the monopile can be considered as a joint with multiple holes that are loaded by pins. In the literature, the stress concentration factors for circular pinned joints with multiple pins can be found as a function of the geometry's dimensions (Pilkey et al., 2020). It is noted that the shape of the holes in the monopile for the wedge connection design is not circular, and also the preloaded fasteners change the deformation level and subsequently the stress concentration. For these reasons, the solutions provided here are an approximation.

Some research has been undertaken into the effect of the shape of the pin on the stress concentration factor for single lap joints made of composite materials. This research found that a 'race-track' shaped pin reduces the stress concentration factor when compared with a circular pin by up to 28% (Zhou et al., 2016). This factor is not directly applicable to this case as the shape of the holes in the case of the current wedge connection design is not 'race-track' (although they are more similar to this than the circular holes), and the material in this case is not a composite, and the joints are double rather than single lap. However, this research suggested that the use of SCF data for circular holes is a conservative approach, as a higher SCF assumed will lead to poorer predicted fatigue performance.

In the case of the wedge connection design considered in the present study, firstly the ratio e/d is considered where e is the distance from the edge of the plate to the top of the hole and d is the hole diameter. From Fig. 18 it can be seen that in a single wedge connection segment considered in this study the distance e is 102 mm. There are two radii of curvature associated with the curved portion of the hole where the wedge assembly sits. Therefore, the diameter d can be taken as either $115\,mm$ or $101\,mm$, so e/d is 0.9 or 1.0, respectively, hence given the available curves in Reference (Pilkey et al., 2020) for circular pinned joints, e/d will be taken as equal to unity.

Extracting the data from Reference (Pilkey et al., 2020) for $e/d = 1$ and adding in a cubic line of best fit gives the solution of SCF, K_{tnb}, described using Equation (51). In this case, $l = \pi D/n$, where n is the number of connections and D is the diameter of the monopile, therefore $d/l = dn/\pi D$.

$$K_{tnb} = 2.95\left(\frac{d}{l}\right)^3 + 0.49\left(\frac{d}{l}\right)^2 + 0.24\left(\frac{d}{l}\right) + 1.09 \qquad \text{Equation(51)}$$

The literature gives that for a nominal stress $\sigma_{nom} = P/d$ on one pin, the maximal stress in the plate will be $\sigma_{max} = K_{tnb}\sigma_{nom} = K_{tnb}P/d$. The assumption is that, for a given d, the nominal stress on each pin remains fixed as l varies. However, in this case, as the number of connections varies, the nominal stress on each pin also varies.

Therefore, here the stress concentration factor $K(n)$ is looked to be found, where the maximal stress on the monopile is $\sigma K(n)$, where σ is the stress around the whole circumference of the monopile. Suppose that the applied tensile force is F_A. Then σ can be approximated as $F_A/\pi Dw$, where w is the width of the monopile's wall. The nominal stress on one connection will therefore be $(F_A/n)/(wd) = F_A/nwd$. Hence:

$$\sigma_{max} = K_{tnb}\sigma_{nom} = K_{tnb}\frac{F_A}{nwd} = \left(\frac{K_{tnb}\pi D}{nd}\right)\left(\frac{F_A}{\pi Dw}\right) = \left(\frac{K_{tnb}\pi D}{nd}\right)\sigma$$

Equation(52)

Therefore:

$$\begin{aligned} K(n) &= \frac{K_{tnb}\pi D}{nd} = \frac{\pi D}{nd}\left(2.95\left(\frac{d}{l}\right)^3 + 0.49\left(\frac{d}{l}\right)^2 + 0.24\left(\frac{d}{l}\right) + 1.09\right) \\ &= \frac{\pi D}{nd}\left(2.95\left(\frac{dn}{\pi D}\right)^3 + 0.49\left(\frac{dn}{\pi D}\right)^2 + 0.24\left(\frac{dn}{\pi D}\right) + 1.09\right) \\ &= 2.95\left(\frac{d}{\pi D}\right)^2 n^2 + 0.49\frac{d}{\pi D}n + 0.24 + \frac{1.09\pi D}{nd} \end{aligned}$$

Equation(53)

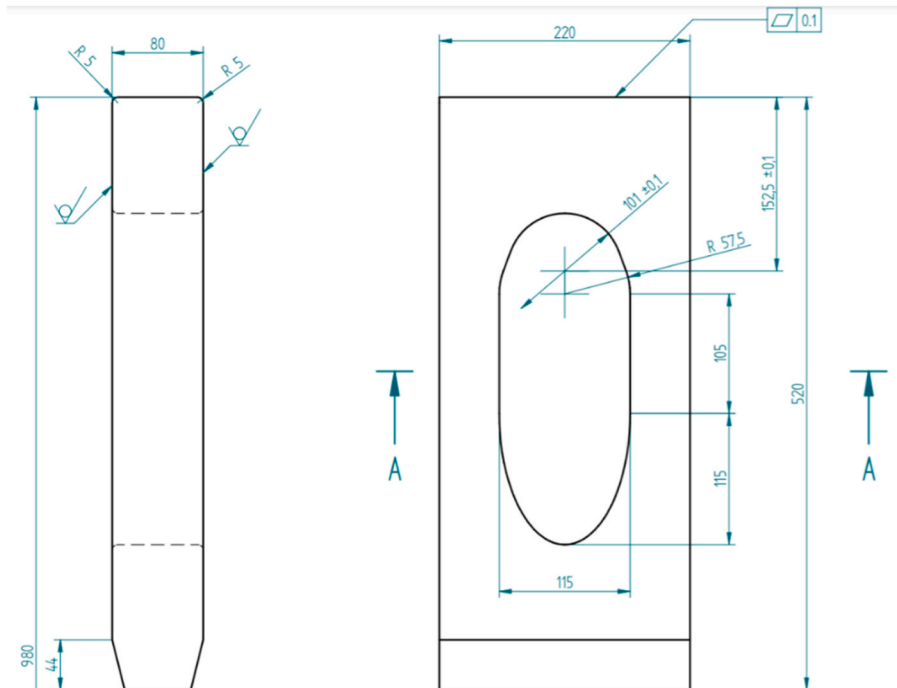To find the minimum value in this expression, the differential is set to zero:

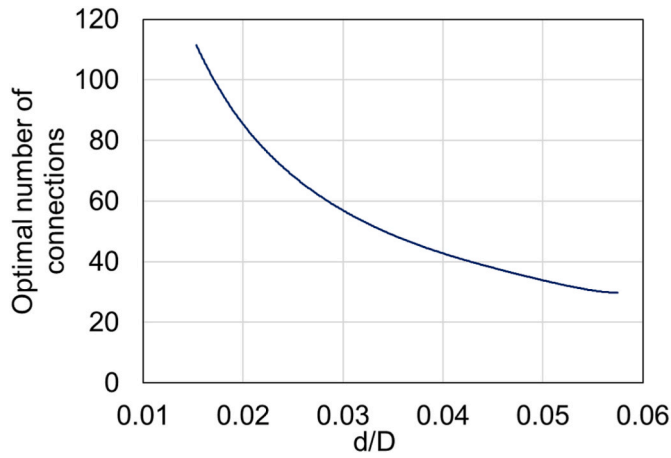Fig. 18. Dimensions of the design of the monopile in a single wedge connection segment (in mm).

Fig. 19. The relationship between the ratio *d/D* and the optimal number of connections.
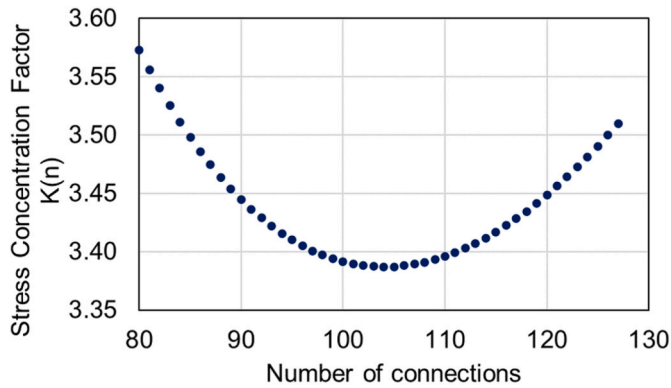

Fig. 20. Stress concentration factor *K(n)* versus the number of connections for $D = 7m$ and $d = 0.115m$.

$$\frac{dK}{dn} = 5.89\left(\frac{d}{\pi D}\right)^2 n + 0.49\frac{d}{\pi D} - \frac{1.09\pi D}{dn^2} = 0 \qquad \text{Equation(54)}$$

$$5.89\left(\frac{d}{\pi D}\right)^2 n^3 + 0.49\frac{d}{\pi D}n^2 - \frac{1.09\pi D}{d} = 0 \qquad \text{Equation(55)}$$

The discriminant of a cubic $a_1 x^3 + a_2 x^2 + a_3 x + a_4$ is:

$$18a_1 a_2 a_3 a_4 - 4a_2^3 a_4 + a_2^2 a_3^2 - 4a_1 a_3^3 - 27a_1^2 a_4^2 \qquad \text{Equation(56)}$$

And in this case $c = 0$, therefore the discriminant is $-4a_2^3 a_4 - 27a_1^2 a_4^2$ which is negative since $a_1 = 5.89(d/\pi D)^2 > 0$ and $0.49\frac{d}{\pi D} > 0$, hence there is only one real solution. The nearest integer to this solution provides the answer to the optimal (i.e. minimal) number of connections. Fig. 19 shows the relationship between the ratio *d/D* and the optimal number of connections. In the case where $d = 115mm$ and $D = 7m$, it can be seen that $n = 104$. Fig. 20 shows the relationship between $K(n)$ and the number of connections *n* for $d = 115mm$ and $D = 7m$.

It is now shown that the minimal value of $K(n)$ does not depend on d/D. It can be seen that:

$$K(n) = \frac{2.95}{\pi^2}\left(\frac{d}{D}n\right)^2 + \frac{0.49}{\pi}\left(\frac{d}{D}n\right) + 0.24 + \frac{1.09\pi}{\left(\frac{d}{D}n\right)} = \frac{2.95}{\pi^2}\tilde{n}^2 + \frac{0.49}{\pi}\tilde{n} + 0.24$$

$$+ \frac{1.09\pi}{\tilde{n}}$$

$$\text{Equation(57)}$$

where $\tilde{n} = \frac{d}{D}n$. Let:

$$f(n) = \frac{2.95}{\pi^2}n^2 + \frac{0.49}{\pi}n + 0.24 + \frac{1.09\pi}{n} \qquad \text{Equation(58)}$$

So $K(n) = f\left(\frac{d}{D}n\right)$. Then, to minimise $K(n)$ we differentiate and set to zero:

$$\frac{dK}{dn} = \frac{d}{D}f'\left(\frac{d}{D}n\right) = 0 \qquad \text{Equation(59)}$$

$$f'(\tilde{n}) = 0 \qquad \text{Equation(60)}$$

There is some $\tilde{n}_0$, independent of $\frac{d}{D}$ for which $f'(\tilde{n}_0) = 0$. This $\tilde{n}_0$ minimises $f(\tilde{n}_0) = K(n)$. Hence the minimal value of $K(n)$ is constant and has been calculated to be 3.38. Therefore, according to the assumptions in this analysis, the minimal stress concentration factor that can be achieved is 3.38. As discussed above, this factor is likely to be conservative given that the analysis is based on circular holes.

Similarly, the optimal value of d/l is fixed and takes value 0.543, which is an extrapolation of 8.6% beyond the range of existing data taken from Reference (Pilkey et al., 2020). This relatively small extrapolation helps increase confidence in the approximation. Therefore, $l = 1.84d$, and so the gaps between the holes should be 0.84 times the width of the holes. This fixed optimal value of d/l allows for the calculation of the following simple expression for the optimal number of connections:

$$0.543 = \frac{d}{l} = \frac{dn}{\pi D} \qquad \text{Equation(61)}$$

$$n = \left[\frac{0.543\pi D}{d}\right] \qquad \text{Equation(62)}$$

where the term in square brackets [] denotes the nearest integer to the value calculated using Equation (62).

4.2. SCF calculation via FEM

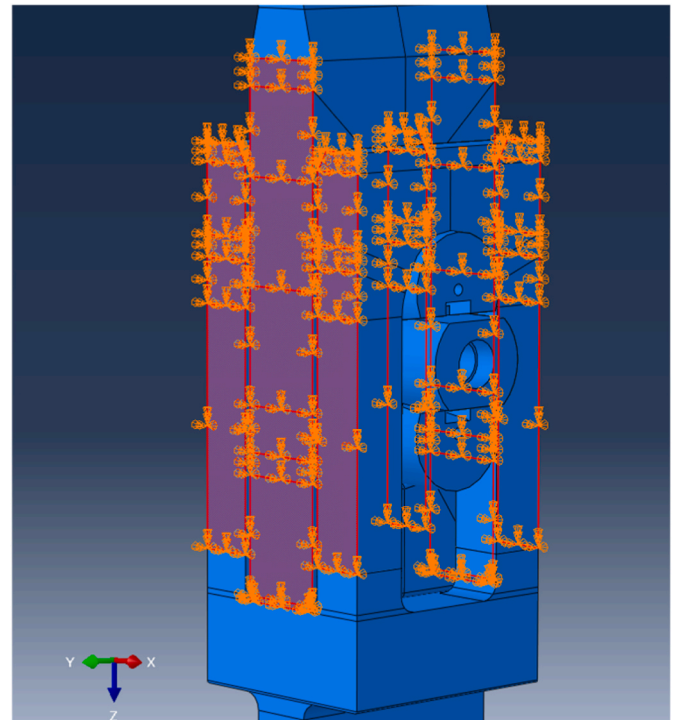FEM analysis has also been undertaken to estimate the SCF in the

Fig. 21. Boundary conditions in FEM simulation.

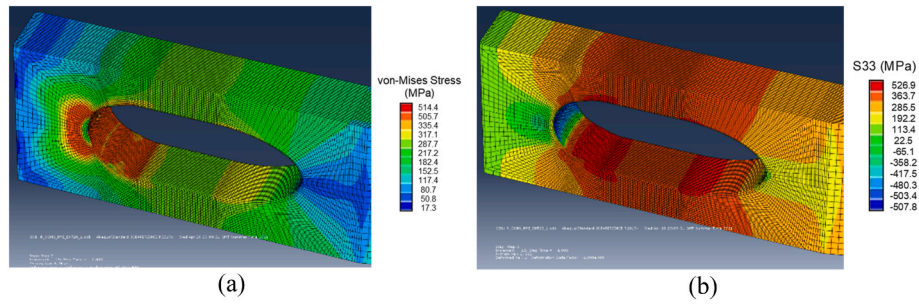(a)   (b)

Fig. 22. Results of (a) the von-Mises stress, and (b) the S33 stress distribution in the FEM model utilising Y-symmetry boundary conditions.

wedge connection segment considered in this study. When a part of the full structure, the deformation of the side faces of monopile and transition piece will be restricted because each of them belongs to an integrated circular structure. To achieve this constraint, the symmetry boundary condition (YSYMM) was applied at the side surfaces of both lower flange and upper flange as shown in Fig. 21.

The resulting von-Mises stress distribution and the axial stress along the loading direction (i.e. S33) are shown in Fig. 22. The highest stress value achieved from the FEM simulation is 373.8 MPa in the critical region. The nominal stress can be found by dividing the load applied in the simulation, 2.3 MN, by the cross-sectional area, which is 80 mm × 220 mm. Therefore, the nominal stress is 130.68 MPa. From this, the SCF value found by dividing the maximal stress by the nominal stress is 2.86. This is lower than the 3.38 value found via the analytical approach detailed in Section 4.1, where circular shaped holes were assumed in calculations. Hence the results presented in Section 4.1 can be considered conservative for design purposes.

4.3. SCF in single connection versus full structure

The SCF minimisation that was investigated in Section 4.1 was for an infinite plate with evenly spaced holes, approximating the full structure. In this section, further consideration is given to comparing optimal SCF in the full structure and optimal SCF in a single connection. This is particularly important due to the fact that a single wedge connection segment is more likely to be the subject of laboratory testing.

This is firstly undertaken by considering approximated versions of both cases. The former as in Section 4.1, the latter by considering a plate of finite width with single circular loaded pin. The literature provides SCF for this secondary case as a function of the ratio d/H, where d is the width of the hole and H is the width of the plate (Pilkey et al., 2020). The definition of nominal stress is given by,

$$\sigma_{nd} = \frac{P}{(H-d)h} \qquad \text{Equation(63)}$$

where P is the load and h is the depth of the plate. In the present study, the nominal stress is defined as $\sigma_{nom} = P/Hh$. Therefore, the aim is to find K such that $\sigma_{max} = K\sigma_{nom}$. Pilkey et al. provide data for K_{tnb} (Pilkey et al., 2020), where:

$$\sigma_{max} = K_{tnb}\sigma_{nb} = K_{tnb}\frac{P}{dh} = \frac{K_{tnb}H}{d}\frac{P}{Hh} = \frac{K_{tnb}H}{d}\sigma_{nom} \qquad \text{Equation(64)}$$

Therefore, $K = K_{tnb}H/d$.

A polynomial fit to the K_{tnb} solutions provided in (Pilkey et al., 2020) gives the following equation for K_{tnb}:

$$K_{tnb} = 66.359\left(\frac{d}{H}\right)^4 - 87.251\left(\frac{d}{H}\right)^3 + 47.851\left(\frac{d}{H}\right)^2 - 8.7243\left(\frac{d}{H}\right) + 1.7347$$

$$\text{Equation(65)}$$

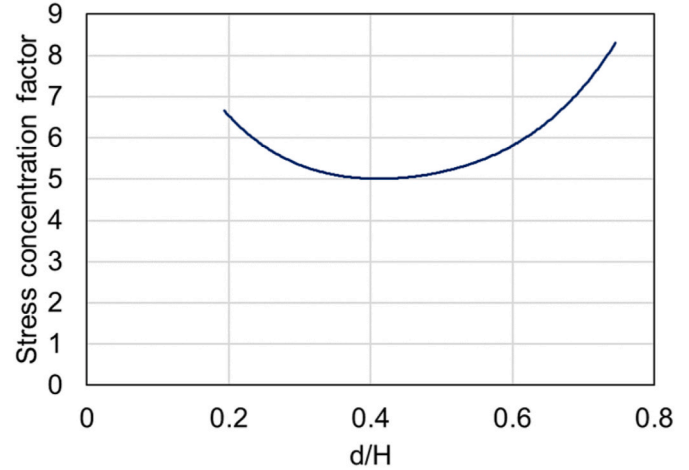Therefore, the following equation for K can be deduced:

Fig. 23. SCF in a plate of finite width with a circular loaded pin as a function of the hole width to plate width ratio, d/H.
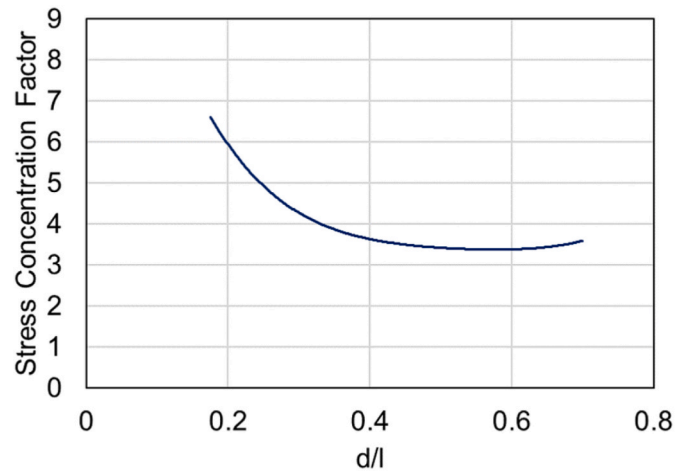
Fig. 24. SCF in a plate of infinite width with evenly spaced circular loaded pins as a function of hole width to distance between pins ratio d/l.

$$K = K_{tnb}\frac{H}{d} = 66.359\left(\frac{d}{H}\right)^3 - 87.251\left(\frac{d}{H}\right)^2 + 47.851\left(\frac{d}{H}\right) - 8.7243$$

$$+ 1.7347\left(\frac{d}{H}\right)^{-1}$$

$$\text{Equation(66)}$$

Differentiating with respect to d/H gives:

$$\frac{dK}{d\left(\frac{d}{H}\right)} = 199.08\left(\frac{d}{H}\right)^2 - 174.50\left(\frac{d}{H}\right) + 47.851 - 1.7347\left(\frac{d}{H}\right)^{-2} = 0$$

Equation(67)

Solving this quartic gives the $d/H = 0.424$, and a minimal SCF of $K = 5.03$. The comparison of the SCF solutions in a plate of finite width with a circular loaded pin as a function of the hole width to plate width ratio, d/H, with a plate of infinite width with evenly spaced circular loaded pins as a function of hole width to distance between pins ratio, d/l, is shown in Figs. 23 and 24, respectively. Comparison of the obtained results show that the optimal SCF that can be achieved in a plate of finite width with a loaded circular pin is 5.03, whilst in an infinite plate with infinite spaced loaded circular pins the optimal SCF is 3.38.

Investigation has also been done using FEM. A simulation was run without the symmetry boundary conditions, thereby better replicating a segment of the wedge connection which is likely to be used for laboratory experiment purposes. The maximal stress was found in the same region and had a value of 405.3 MPa. Therefore, the SCF was 3.10, greater than the 2.86 predicted by the prior simulation. Therefore, both the analytical analysis and FEM simulations indicate that any investigation of the fatigue life of a single segment of wedge connection will involve a higher SCF value than the full structure and is therefore likely to be conservative. Further research could involve FEM analysis of the full structure and of the single connection and create a function mapping the behaviour of the single connection to that of the full structure. Any laboratory-based experiments on a single connection could then be robustly mapped onto anticipated behaviour in the full structure.

5. Conclusions

The offshore wind turbine foundation is a cost-critical component of the structure, and analysis of globally installed offshore wind turbines found monopiles to be the dominant foundation type. Optimal MP-TP connection designs therefore have the potential for a high economic impact. Analytical and FEM analyses were undertaken in this study on the newly developed wedge connection MP-TP technology. In the analytical part of the analysis a spring model was designed and solved for both the application of the preload and the combination of the preload and the external force. A comparison was made with the FEM results and found just a 2.28% difference in the calculated preload force. A lower bound on the preload, that would ensure the connection does not become loose, was found from this study. The force felt on the bolts in the wedge connection was calculated and it was concluded that the lateral bolts are not a critical component of the wedge connection, hence self-locking is not a required design feature. Further analytical investigations were carried out to identify the optimal number of wedge connections in one structure in order to minimise the SCF, as a function of the ratio of hole width to monopile diameter. Moreover, it has been demonstrated that the SCF in a single segment of the wedge connection, which is likely to be used for fatigue testing purposes, is higher than in the full wind turbine structure, hence that laboratory experiments on one wedge connection segment are likely to be conservative and therefore suitable for design purposes. Further research in future work could involve undertaking FEM modelling of the full MP-TP structure and varying the number of wedge connections to generate the SCF as a more accurate function of the number of connections. This may provide a more robust assessment of the optimal number of connections and the minimal stress concentration factor achieved from analytical solutions presented in this work.

CRediT authorship contribution statement

Helen Ryan: Conceptualization, Methodology, Validation, Formal analysis, Writing – original draft. **Alessandro Annoni:** Validation, Formal analysis, Writing – review & editing. **Jasper Winkes:** Validation, Resources, Writing – review & editing. **Ali Mehmanparast:** Conceptualization, Resources, Writing – review & editing, Supervision.

Declaration of competing interest

The authors declare that they have no known competing financial interests or personal relationships that could have appeared to influence the work reported in this paper.

Data availability

Data will be made available on request.

Acknowledgments

APPENDICES.

Appendix A. Estimation of spring constants via FEM

In every case, the maximal deformation in the relevant range in the axis of applied force was taken, i.e., the maximal value of U3 in the relevant range.
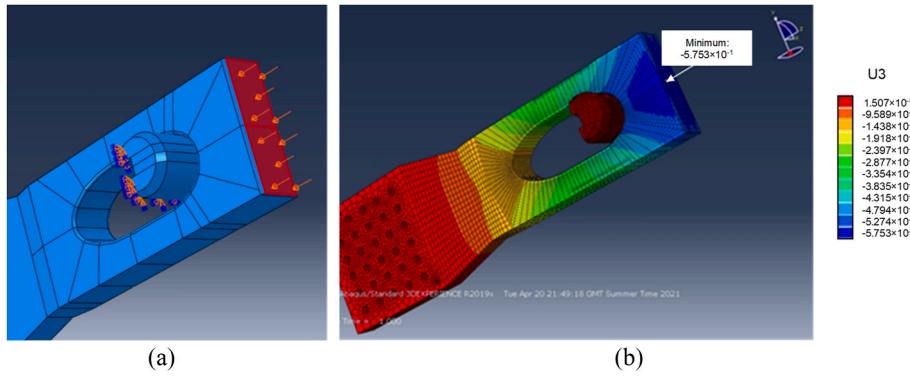
1.1 Spring Constant K_{MP1}

Fig. A-1. (a) Location of boundary conditions and (b) maximal deformation for K_{MP1} estimation

A fully elastic simulation was run with the lower flange and the upper block. The block was made infinitely stiff, and the bottom face of the block was fixed in all degrees of freedom. A force of 2.3 MN was then applied to the top face of the lower flange, as shown in Figure A-1. The maximal deformation in the MP1 spring range was 0.575 mm, therefore K_{MP1} is estimated as:

$$K_{MP1} = \frac{2.3}{0.575} = 4.00 \; MN \Big/ mm \qquad \qquad \text{Equation(A-1)}$$

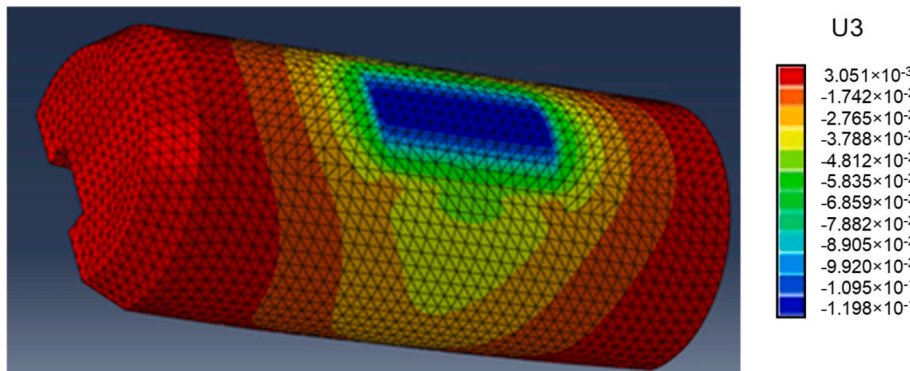*1.2 Spring Constants K_{B1} and K_{B2}*

Fig. A-2. U3 deformation on the upper block in spring constant simulation

The upper and lower block spring constants were assumed to be equal. The same simulation was run as in the estimation of K_{MP1}, but with the monopile made infinitely stiff and the upper block with its usual Elastic Young's modulus. The maximal deformation in the axis of the applied force on the block was 0.120 mm, as shown in Figure A-2. Therefore, the spring constants were estimated as:

$$K_{B1} = K_{B2} = \frac{2.3}{0.120} = 18.9 \; MN \Big/ mm \qquad \qquad \text{Equation(A-2)}$$
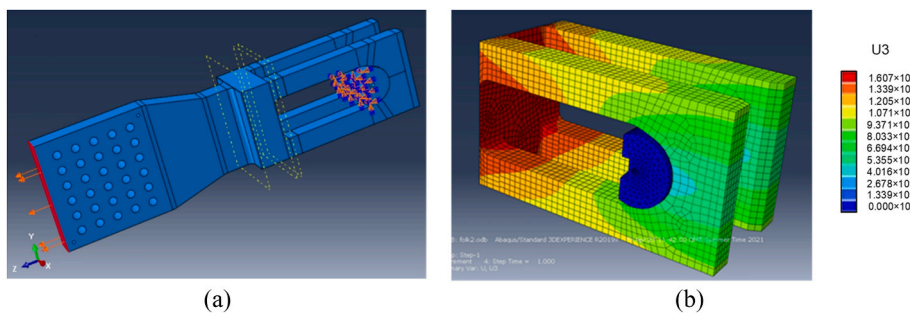
1.3 Spring Constant K_{TP}

Fig.A-3. (a) Location of boundary conditions and (b) maximal deformation for K_{TP} estimation

A fully elastic simulation was run with the transition piece and the lower block. The block was made infinitely stiff, and the bottom face of the block

was fixed in all degrees of freedom. A force of 2.3 MN was then applied to the bottom of the transition piece, as shown in Figure A-3. The top of the hole deformed by 1.61 mm, as shown in Figure A-3, and the bottom of the hole deformed in the same direction by 0.50 mm. Therefore, the overall maximal deformation in the TP spring range was 1.61–0.50 = 1.11 mm. The spring constant can therefore be estimated:

$$K_{TP} = \frac{2.3}{1.11} = 2.07 \; MN \Big/ mm \qquad \qquad \text{Equation(A-3)}$$

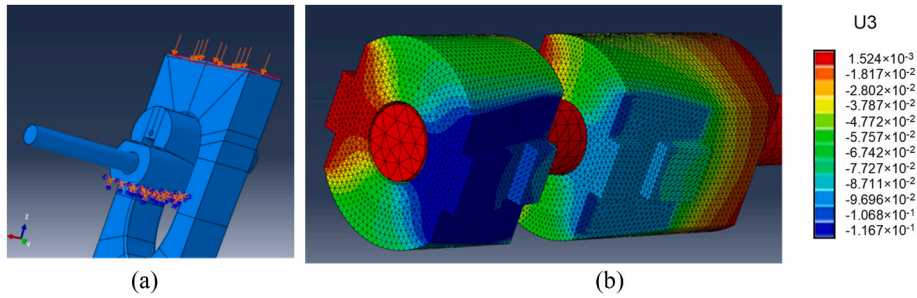*1.4 Spring Constant K_W*

Fig. A-4. (a) Location of boundary conditions and (b) maximal deformation for K_W estimation

A fully elastic simulation was run with the monopile, the upper block, and the wedges. The monopile and block were made infinitely stiff, and the bottom faces of the wedges were fixed in all degrees of freedom. A force of 2.3 MN was then applied to the top of the monopile, as shown in Figure A-4. The maximal compression of the wedges was 0.117 mm, as shown in Figure A-4. The spring constant can therefore be estimated:

$$K_W = \frac{2.3}{0.117} = 19.7 \; MN \Big/ mm \qquad \qquad \text{Equation(A-4)}$$

1.5 Spring Constant K_{MP2}

To estimate K_{MP2}, the *MP*2 section was split into two springs in series, *MP*3 and *MP*4, as shown in Figure A-5.
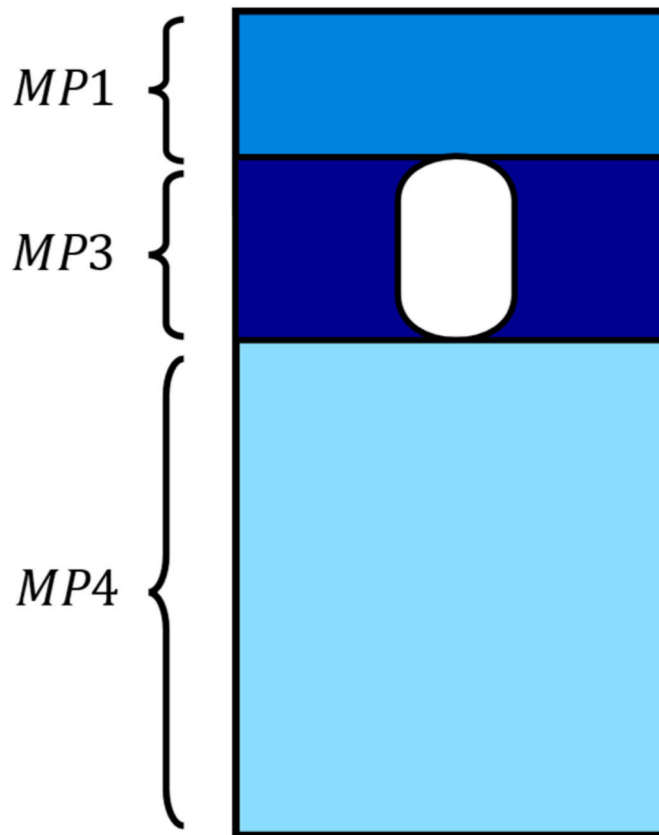

Fig. A-5. Springs MP1, MP3 and MP4

K_{MP3} can be estimated from FEM. However, the spring *MP4* does not really exist in the geometry analysed in FEM. Therefore, MP4 is analysed analytically.

Considering first K_{MP3}, a fully elastic simulation was run with the lower flange and the upper block. The block was made infinitely stiff, and the bottom face of the block was fixed in all degrees of freedom. A force of 2.3 MN was then applied to the bottom face of the lower flange, as shown in Figure A-6. The top of the hole deformed by 1.57 mm, as shown in Figure A-6, and the bottom of the hole deformed in the same direction by 0.52 mm. Therefore, the overall maximal deformation in the *MP3* spring range was 1.57–0.52 = 1.05 mm. The spring constant can therefore be estimated:

$$K_{MP3} = \frac{2.3}{1.05} = 2.19 \; MN \Big/ mm \qquad \text{Equation(A-5)}$$
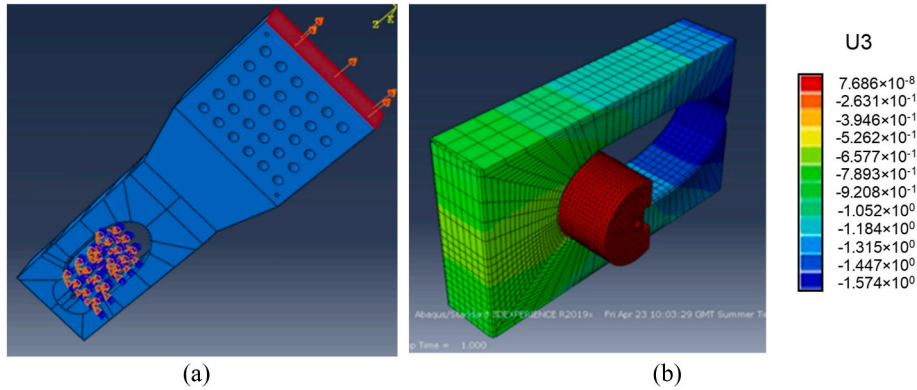

Fig. A-6. (a) Location of boundary conditions and (b) maximal deformation for K_{MP3} estimation

The spring *MP4* can be approximated as a simple plate. It will be assumed that the monopile has length of 25m and the plate has width 220 mm and depth 80 mm, so the cross-sectional area would be 17,600 mm^2. The spring constant can then simply be estimated via the elastic Young's modulus *E*:

$$K_{MP4} = E \cdot \frac{17600}{25000} = 212000 \cdot \frac{17600}{25000} = 0.149 \; MN \Big/ mm \qquad \text{Equation(A-6)}$$

Finally, K_{MP2} can then be estimated from K_{MP3} and K_{MP4}:

$$K_{MP2} = \frac{1}{\frac{1}{K_{MP3}} + \frac{1}{K_{MP4}}} = 0.140 \; MN \Big/ mm \qquad \text{Equation(A-7)}$$

Appendix B. Solution to spring system with externally applied axial force

The method for finding the solution to the system described in Section 3.5 is provided here. The energy of the system is:

$$\mathrm{E} = F_A \tilde{x}_1 + \frac{K_{MP1}}{2}(\tilde{x}_1 - \tilde{x}_2)^2 + \frac{K_{B1}}{2}(\tilde{x}_2 - \tilde{x}_4)^2 \frac{K_W}{2}(\tilde{x}_4 - \tilde{x}_5 - 2y_0)^2 + \frac{K_{B2}}{2}(\tilde{x}_5 - \tilde{x}_7)^2 + \frac{K_{TP}}{2}(\tilde{x}_1 - \tilde{x}_7)^2 + \frac{K_{MP2}}{2}\widetilde{x_2}^2 \qquad \text{Equation(B-1)}$$

This gives rise to the following system of linear equations:

$$\begin{pmatrix} K_{MP1} + K_{TP} & -K_{MP1} & 0 & 0 & -K_{TP} \\ -K_{MP1} & K_{MP1} + K_{B1} + K_{MP2} & -K_{B1} & 0 & 0 \\ 0 & -K_{B1} & K_{B1} + K_W & -K_W & 0 \\ 0 & 0 & -K_W & K_W + K_{B2} & -K_{B2} \\ -K_{TP} & 0 & 0 & -K_{B2} & K_{B2} + K_{TP} \end{pmatrix} \begin{pmatrix} \tilde{x}_1 \\ \tilde{x}_2 \\ \tilde{x}_4 \\ \tilde{x}_5 \\ \tilde{x}_7 \end{pmatrix} = \begin{pmatrix} F_A \\ 0 \\ 2K_W y_0 \\ -K_W y_0 \\ 0 \end{pmatrix} \qquad \text{Equation(B-2)}$$

Solving this system, by multiplying both sides of the equation by K^{-1} matrix, gives the following solutions:

$$\tilde{x}_1 = (F_A(K_{B1}K_{B2}K_{MP1}K_{TP} + K_{B1}K_{B2}K_{MP2}K_{TP} + K_{B1}K_{B2}K_{MP1}K_W + K_{B1}K_{B2}K_{MP1}K_W + K_{B1}K_{B2}K_{MP2}K_W + K_{B1}K_{B1}K_{TP}K_W + K_{B1}K_{MP1}K_{TP}K_W + K_{B1}K_{MP2}K_{TP}K_W$$
$$+ K_{B2}K_{MP1}K_{TP}K_W + K_{B2}K_{MP2}K_{TP}K_W) - 2y_0 K_{B1}K_{B2}K_{MP2}K_{TP}K_W)$$
$$\Big/ \; (K_{B1}K_{B2}K_{MP1}K_{MP2}K_{TP} + K_{B1}K_{B2}K_{MP1}K_{MP2}K_W + K_{B1}K_{B2}K_{MP2}K_{TP}K_W + K_{B1}K_{MP1}K_{MP2}K_{TP}K_W + K_{B2}K_{MP1}K_{MP2}K_{TP}K_W)$$

$$\text{Equation(B-3)}$$

$$\tilde{x}_2 = \frac{F_A}{K_{MP2}} \qquad \text{Equation(B-4)}$$

$$\widetilde{x_4} = (F_A(K_{B1}K_{B2}K_{MP1}K_{TP} + K_{B1}K_{B2}K_{MP1}K_W + K_{B1}K_{B2}K_{MP1}K_W + K_{B1}K_{B1}K_{TP}K_W + K_{B1}K_{MP1}K_{TP}K_W + K_{B2}K_{MP1}K_{TP}K_W) + 2y_0 K_{MP1}K_{B2}K_{MP2}K_{TP}K_W)$$
$$/ (K_{B1}K_{B2}K_{MP1}K_{MP2}K_{TP} + K_{B1}K_{B2}K_{MP1}K_{MP2}K_W + K_{B1}K_{B2}K_{MP2}K_{TP}K_W + K_{B1}K_{MP1}K_{MP2}K_{TP}K_W + K_{B2}K_{MP1}K_{MP2}K_{TP}K_W)$$

Equation(B-5)

$$\widetilde{x_5} = (F_A(K_{B1}K_{B2}K_{MP1}K_{TP} + K_{B1}K_{B2}K_{MP2}K_{TP} + K_{B1}K_{B2}K_{MP1}K_W + K_{B1}K_{B2}K_{TP}K_W + K_{B1}K_{MP1}K_{TP}K_W + K_{B2}K_{MP1}K_{TP}K_W + K_{B2}K_{MP2}K_{TP}K_W)$$
$$- 2y_0(K_{B1}K_{B2}K_{MP1}K_{MP2}K_W + K_{B1}K_{B2}K_{MP2}K_{TP}K_W + K_{B1}K_{MP1}K_{MP2}K_{TP}K_W))$$
$$/ (K_{B1}K_{B2}K_{MP1}K_{MP2}K_{TP} + K_{B1}K_{B2}K_{MP1}K_{MP2}K_W + K_{B1}K_{B2}K_{MP2}K_{TP}K_W + K_{B1}K_{MP1}K_{MP2}K_{TP}K_W + K_{B2}K_{MP1}K_{MP2}K_{TP}K_W)$$

Equation(B-6)

$$\widetilde{x_7} = (F_A(K_{B1}K_{B2}K_{MP1}K_{TP} + K_{B1}K_{B2}K_{MP2}K_{TP} + K_{B1}K_{B2}K_{MP1}K_W + K_{B1}K_{B2}K_{TP}K_W + K_{B1}K_{MP1}K_{TP}K_W + K_{B1}K_{MP2}K_{TP}K_W + K_{B2}K_{MP1}K_{TP}K_W + K_{B2}K_{MP2}K_{TP}K_W)$$
$$- 2y_0(K_{B1}K_{B2}K_{MP1}K_{MP2}K_W + K_{B1}K_{B2}K_{MP2}K_{TP}K_W))$$
$$/ (K_{B1}K_{B2}K_{MP1}K_{MP2}K_{TP} + K_{B1}K_{B2}K_{MP1}K_{MP2}K_W + K_{B1}K_{B2}K_{MP2}K_{TP}K_W + K_{B1}K_{MP1}K_{MP2}K_{TP}K_W + K_{B2}K_{MP1}K_{MP2}K_{TP}K_W)$$

Equation(B-7)

Let $\widetilde{\delta_i}$ denote the new expansion (or compression) of spring $i \in C$. Then the solution can be simplified as follows:

$$\widetilde{\delta}_{MP1} = (F_A(K_{B1}K_{B2}K_{MP2}K_{TP} + K_{B1}K_{B2}K_{MP2}K_W + K_{B1}K_{MP2}K_{TP}K_W + K_{B2}K_{MP2}K_{TP}K_W) - 2y_0 K_{B1}K_{B2}K_{MP2}K_{TP}K_W)$$
$$/ (K_{B1}K_{B2}K_{MP1}K_{MP2}K_{TP} + K_{B1}K_{B2}K_{MP1}K_{MP2}K_W + K_{B1}K_{B2}K_{MP2}K_{TP}K_W + K_{B1}K_{MP1}K_{MP2}K_{TP}K_W + K_{B2}K_{MP1}K_{MP2}K_{TP}K_W)$$

Equation(B-8)

Dividing top and bottom by $\prod_{i \in C} K_i$ gives:

$$\widetilde{\delta}_{MP1} = \frac{\frac{F_A}{K_{MP1}}\left(\frac{1}{K_W} + \frac{1}{K_{TP}} + \frac{1}{K_{B1}} + \frac{1}{K_{B2}}\right) - \frac{2y_0}{K_{MP1}}}{K_{DOM}}$$

Equation(B-9)

$$\widetilde{\delta}_{MP1} = \frac{\frac{F_A}{K_{MP1}}\left(K_{DOM} - \frac{1}{K_{MP1}}\right)}{K_{DOM}} + \delta_{MP1} = \frac{1}{K_{MP1}}\left(\frac{F_A\left(K_{DOM} - \frac{1}{K_{MP1}}\right)}{K_{DOM}} - PL\right) = \frac{1}{K_{MP1}}\left(F_A - \frac{F_A}{K_{DOM}K_{MP1}} - PL\right) = -0.102\ mm$$

Equation(B-10)

Similarly, the following are calculated, and evaluated for the case that $F_A = 2.3\ MN$ and $x_0 = 6.5$:

$$\widetilde{\delta}_{TP} = \widetilde{x_1} - \widetilde{x_7} = \frac{\frac{F_A}{K_{MP1}}\left(\frac{1}{K_{TP}}\right)}{K_{DOM}} + \delta_{TP} = \frac{1}{K_{TP}}\left(\frac{F_A}{K_{MP1}K_{DOM}} + PL\right) = 1.30\ mm$$

Equation(B-11)

$$\widetilde{\delta}_{B1} = \widetilde{x_2} - \widetilde{x_4} = \frac{-\frac{F_A}{K_{MP1}}\left(\frac{1}{K_{B1}}\right)}{K_{DOM}} + \delta_{B1} = -\frac{1}{K_{B1}}\left(\frac{F_A}{K_{MP1}K_{DOM}} + PL\right) = -0.143\ mm$$

Equation(B-12)

$$\widetilde{\delta}_{B2} = \widetilde{x_2} - \widetilde{x_4} = \frac{-\frac{F_A}{K_{MP1}}\left(\frac{1}{K_{B2}}\right)}{K_{DOM}} + \delta_{B2} = -\frac{1}{K_{B2}}\left(\frac{F_A}{K_{MP1}K_{DOM}} + PL\right) = -0.143\ mm$$

Equation(B-13)

$$\widetilde{\delta}_W = \widetilde{x_2} - \widetilde{x_4} = \frac{-\frac{F_A}{K_{MP1}}\left(\frac{1}{K_W}\right)}{K_{DOM}} + \delta_W = -\frac{1}{K_W}\left(\frac{F_A}{K_{MP1}K_{DOM}} + PL\right) = 0.137\ mm$$

Equation(B-14)

$$\widetilde{\delta}_{MP2} = \widetilde{x_2} = \frac{F_A}{K_{MP2}} = 16.4\ mm$$

Equation(B-15)

References

Anandavijayan, S., Mehmanparast, A., Braithwaite, J., Brennan, F., Chahardehi, A., 2021. Material pre-straining effects on fatigue behaviour of S355 structural steel. J. Constr. Steel Res. 183, 106707.

Arredondo-Galeana, A., Brennan, F., 2021. Floating offshore vertical axis wind turbines: opportunities, challenges and way forward. Energies 14 (23), 8000.

Bhattacharya, S., 2019. Design of Foundations for Offshore Wind Turbines, first ed. Wiley, Hoboken, NJ, USA.

Braithwaite, J., Mehmanparast, A., 2019. Analysis of tightening sequence effects on preload behaviour of offshore wind turbine M72 bolted connections. Energies 12 (23), 4406.

Braithwaite, J., Goenaga, I.G., Tafazzoli moghaddam, B., Mehmanparast, A., 2020. Sensitivity analysis of friction and creep deformation effects on preload relaxation in offshore wind turbine bolted connections. Appl. Ocean Res. 101, 102225.

Crescimanno, P.J., Keller, K., 1981. Forces in Bolted Joints: Analysis Methods and Test Results Utlized for Nuclear Core Applications. University of North Texas Libraries, Pennsylvania.

Creusen, K., 2017. Design and Analysis of a Wedge Connection for Offshore Foundations [Online]. Available: http://resolver.tudelft.nl/uuid:60577283-be1e-40a5-8 606-defd8a355ebe.

Creusen, K.E.Y., Misios, G., Winkes, J.S., Veljkovic, M., 2022. Introducing the C1 wedge connection. Steel Construction 15 (1), 13–25.

Delwiche, A., Tavares, I., 2017. Retrofit Strategy Using Aluminum Anodes for the Internal Sections of Wind Turbine Monopiles. Corrosion 2017, New Orleans.

Díaz, H., Soares, C.G., 2020. Review of the current status, technology and future trends of offshore wind farms. Ocean Eng. 209, 107381.

Díaz, H., Serna, J., Nieto, J., Guedes Soares, C., 2022. Market needs, opportunities and barriers for the floating wind industry. J. Mar. Sci. Eng. 10 (7), 934.

Esteban, M.D., López-Gutiérrez, J.-S., Negro, V., 2019. Gravity-based foundations in the offshore wind sector. J. Mar. Sci. Eng. 64 (7).

EWEA, 2016. The European Offshore Wind Industry - Key Trends and Statistics 2015. European Wind Energy Association.

Goodman, L.E., Warner, W.H., 1963. Dymanics. Dover Publications.

GWEC, 2021. China Installed Half of New Global Offshore Wind Capacity during 2020 in Record Year [Online]. Available: https://gwec.net/china-installed-half-of-new-glo bal-offshore-wind-capacity-during-2020-in-record-year/. (Accessed 14 April 2021).

Handy, N.C., Lee, A.M., 1996. The adiabatic approximation. Chem. Phys. Lett. 252 (5–6), 425–430.

Hao, E., Liu, C., 2017. Evaluation and comparison of anti-impact performance to offshore wind turbine foundations: monopile, tripod, and jacket. Ocean Eng. 130, 218–227.

Hu, Y., Yang, J., Baniotopoulos, C., Wang, X., Deng, X., 2020. Dynamic analysis of offshore steel wind turbine towers subjected to wind, wave and current loading during construction. Ocean Eng. 216, 108084.

Jörss Blunck Ordemann, "World wind technology," [Online]. Available: https://www.windpower-international.com/contractors/world-wind-technology/monopile-foundations-with-flanged-connections. [Accessed 21 04 2021].

Lochan, S., Mehmanparast, A., Wintle, J., 2019. A review of fatigue performance of bolted connections in offshore wind turbines. Procedia Struct. Integr. 17, 276–283.

Mehmanparast, A., Brennan, F., Tavares, I., 2017. Fatigue crack growth rates for offshore wind monopile weldments in air and seawater: SLIC inter-laboratory test results. Mater. Des. 114, 494–504.

Mehmanparast, A., Lotfian, S., Vipin, S.P., 2020. A review of challenges and opportunities associated with bolted flange connections in the offshore wind industry. Metals 10 (6).

Orsted, 2021. Orsted Website [Online]. Available: https://orsted.co.uk/energy-solutions/offshore-wind. (Accessed 20 April 2021).

OVAKO, "Material data sheet, S355JR," [Online]. Available: https://steelnavigator.ovako.com/steel-grades/s355/. [Accessed 10 March 2021].

Pilkey, W.D., Pilkey, D.F., Bi, Z., 2020. Peterson's Stress Concentration Factors, fourth ed. John Wiley & Son.

Redondo, R., Mehmanparast, A., 2020. Numerical analysis of stress distribution in offshore wind turbine M72 bolted connections. Metals 10 (5), 689.

Richards, K.L., 2018. Design Engineer's Sourcebook. CRC Press.

Ryan, H., Mehmanparast, A., 2023. Development of a new approach for corrosion-fatigue analysis of offshore steel structures. Mech. Mater. 176, 104526.

Sánchez, S., López-Gutiérrez, J.-S., Negro, V., Esteban, M.D., 2019. Foundations in offshore wind farms: evolution, characteristics and range of use. Analysis of main dimensional parameters in monopile foundations. J. Mar. Sci. Eng. 7 (12), 441.

Sati, M., Verma, M., 2021. Fundamentals of energy: its potentials and achievements. In: Renewable Energy and Green Technology. CRC Press, pp. 1–12.

Schaumann, P., Eichstädt, R., 2015. Fatigue Assessment of High-Strength Bolts with Very Large Diameter in Substructures for Offshore Wind Turbines. Kona, Big Island, Hawaii, USA.

Soares-Ramos, E.P., de Oliveira-Assis, L., Sarrias-Mena, R., Fernández-Ramírez, L.M., 2020. Current status and future trends of offshore wind power in Europe. Energy 202, 117787.

UK, G.O.V., 2022. Major Acceleration of Homegrown Power in Britain's Plan for Greater Energy Independence [Online]. Available: https://www.gov.uk/government/news/major-acceleration-of-homegrown-power-in-britains-plan-for-greater-energy-independence. (Accessed 22 December 2022).

Vanden Haute, C., Pire, T., 2020. Maintenance intervals for MP-TP bolted connections – a case study. Results in Engineering 5.

Vestas, "2MW V80-2.0 MW, V90-1.8/2.0 MW, V100-1.8 MW," 2011. [Online]. Available: https://www.ledsjovind.se/tolvmanstegen/Vestas%20V90-2MW.pdf. [Accessed 27 April 2021].

Wang, P., Zhao, M., Du, X., Liu, J., Xu, C., 2018. Wind, wave and earthquake responses of offshore wind turbine on monopile foundation in clay. Soil Dynam. Earthq. Eng. 113, 47–57, 0267-7261.

Offshore Wind Innovators, "C1 connections successfully performs full-scale test with the C1 wedge connection," [Online]. Available: https://www.offshorewindinnovators.nl/news/c1-connections-successfully-performs-full-scale-test-with-the-c1-wedge-connection . [Accessed 13 March 2021].

Yu, H., Zeng, X., Li J, B., Lian, 2015. Centrifuge modeling of offshore wind foundations under earthquake loading. Soil Dynam. Earthq. Eng. 77, 402–415.

Zhou, Y., Fei, Q., Fei, Q., 2016. Profile design of loaded pins in composite single lap joints: from circular to non-circular. Results Phys. 6.